We are IntechOpen,
the world's leading publisher of
Open Access books
Built by scientists, for scientists

4,800
Open access books available

122,000
International authors and editors

135M
Downloads

Our authors are among the

154
Countries delivered to

TOP 1%
most cited scientists

12.2%
Contributors from top 500 universities

CLARIVATE ANALYTICS
BOOK CITATION INDEX
INDEXED

WEB OF SCIENCE™

Selection of our books indexed in the Book Citation Index
in Web of Science™ Core Collection (BKCI)

Interested in publishing with us?
Contact book.department@intechopen.com

Numbers displayed above are based on latest data collected.
For more information visit www.intechopen.com

Animal Eyes and Video Imagery

Tomasz P. Jannson and Ranjit Pradhan
Physical Optics Corporation,
USA

1.Introduction

1.1 "Natural engineering", human engineering, and "artificial abstraction"

Nature created a multitude of forms of animal eyes as a manifestation of "natural engineering." *Human engineering* (HE) came much later, creating its own forms of artificial vision or video imagery, some of them as repetitions of *natural engineering* (NE) and some of them as supposed-to-be NE-repetitions (i.e., possibly wrong guesses); these latter we call "*artificial abstractions*" (AAs), being an interesting product of human imagination. This paper is about relationships among these various forms of engineering in respect to animal eyes.

Although the earth has existed for several billion years, the vast majority of animal forms having eyes similar to those in existence today appeared during the so-called *Cambrian explosion,* about 530 million years ago, probably related to development of a new NE-based *concept of operation* (CONOPS): *visually-guided-predation,* which, in turn, created new NE-constructions: larger (macroscopic) animals with hardened tissue. This hardened tissue was necessary to create pigment-based *vignetting effect*, a precursor of animal vision (Fig. 1).

Through the movement of such a primitive eye (through all-body movement), various photoreceptors would receive different optical signals, thus, creating a kind of *spatial* vision. Further NE developments have bifurcated into two basic directions: *apposition* eyes (such as bug eyes) and *imaging* eyes, the latter to be found in almost all vertebrates.

In Section 2, we will discuss one of the first attempts to study the animal eye, Maxwell's "fish-eye," and *aquatic* eyes based on *Graded-Index* (GRIN) optics, including an *Artificial Abstraction* (AA): "fish-eye" *catadioptric* systems.

In Section 3 the recently discovered concept of the lobster eye is reviewed in detail, while in Section 4 both natural vision and artificial color vision are studied.

In Section 5, optical imaging resolution/sensitivity, in the context of animal eyes, are studied, while in Section 6, animal mirrors, vignetting, anti-reflection (AR) structures, total internal reflection, camouflage, and the other natural optical elements are discussed.

In Section 7, a new concept of spectral imaging as a manifestation of HE-based apposition eyes, is introduced.

In Section 8, the neurophysiology of the retina and visual cortex, in the context of video imagery, is analyzed, and, finally, a summary and overall discussion of AA examples, are presented in Section 9.

Abbreviations are reduced to a minimum, although some of them, such as HE, NE, and AA, are used throughout the text for the sake of space. Some others, such as TIR, GRIN, CONOPS are commonly used in engineering literature. Others, containing a great many words, are used only locally for the sake of space.
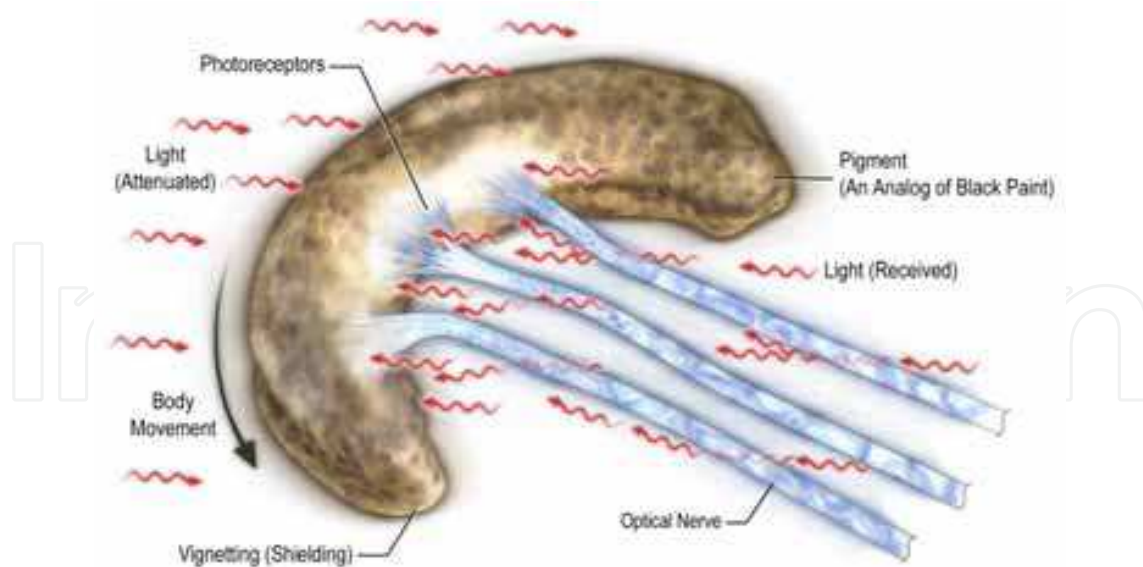
Fig. 1. Illustration of a lensless vision system based on the vignetting effect, a precursor of the animal eye. We see that optical nerves are blocking the view, an unwanted effect to be discussed later, in the context of the human eye

2. Maxwell's "Fish-eye," GRIN lenses, and Aquatic eyes

Starting with apposition eyes (Land & Nilsson, 2002) investigated by Robert Hook in 1665, Maxwell's "fish-eye" in 1854 (Born & Wolf, 1999; Maxwell, 1854), and the Luneburg lens (Luneburg, 1964), in the 1950s, animal eye systems, including *fish-eyes, bug eyes, lobster eyes,* and others, have been adopted for artificial vision. In particular, it has been proven that the lobster eye can be considered an advanced bug eye in biologic evolution. Attractive military and Homeland Security HE applications have been developed, including an IR/visible lobster-eye system as a hemispheric awareness sensor (Grubsky et al., 2006), and an X-ray lobster eye as the first X-ray lens for improvised explosive device (IED) detection and "see through" applications (Gertsenshteyn et al., 2005; Jannson et al., 2006b; Jannson et al., 2007a, and Gertsenshteyn at al., 2007).

The primary concern in mimicking animal eyes, within the scope of geometrical and physical optics, has been connected with so-called *absolute imaging* instruments, which provide precise point-to-point imaging (i.e., without aberrations). Unfortunately, such systems, including the Maxwell fish-eye and Luneburg lens, require 3D Graded-Index distribution, which complicates fabrication. The practical response to these problems has been *catadioptric* systems, which combine the imaging properties of refractive and reflective optics (Baker & Nayar, 1999). While these systems do not preserve absolute imaging properties, they have an almost hemispheric (or, rather, omni-directional) view, sometimes also using the "fish-eye" name.

2.1 Maxwell's "Fish-eye" and the Luneburg Lens
Consider a Graded-Index (GRIN) 3D medium, with spherical symmetry:

$$n(r) = \frac{1}{1 + (r/a)^2} n_o \tag{1}$$

where, a, and n_o are constants, as shown in Fig. 2, where:

$$r = \left(x^2 + y^2 + z^2\right)^{1/2} \quad .$$ (2)

We discuss the ray equation in spherical-coordinates (r, θ), with a solution for: r = a, and $\theta = \alpha$, or $\theta = \pi +$ d. We obtain the one-parameter (α) family of rays,

$$\frac{r^2 - a^2}{r \sin(\theta - \alpha)} = \frac{r_o{}^2 - a_o{}^2}{r_o \sin(\theta_o - \alpha)}$$ (3)
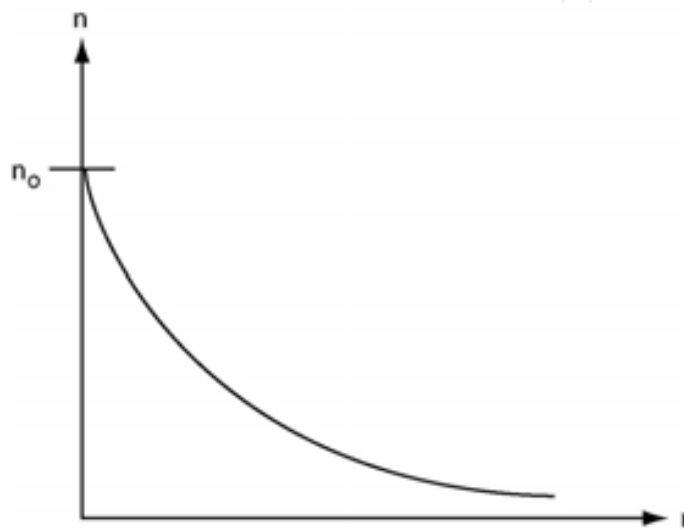

Fig. 2. Illustration of Eq. (1)

This family of rays has two fixed points: $P_o\,(r_o, \theta_o)$, and $P_1(r_1, \theta_1)$, where

$$r_1 = \frac{a^2}{r_o}, \quad \theta_1 = \pi + \theta_o$$ (4ab)

independently on α. Therefore, all the rays pass those two points; thus, the fish-eye is an absolute instrument; this is further discussed in Born & Wolf, 1999, and Jagger, 1992.
The disadvantage of the Maxwell fish-eye is that all media must be GRIN (Graded Index). To avoid this disadvantage, Luneburg designed his lens, also with spherical symmetry, in the form:

$$n(r) = \begin{cases} n(r) = \sqrt{2 - r^2}; & 0 \leq r \leq 1 \\ 1, \; \textit{for } r > 1 \end{cases}$$ (5)

The Luneburg lens's GRIN medium is limited to $r \leq 1$. For any collimated beam passing through this medium, we obtain the focusing into point P_o lying on the medium boundary, shown in Fig. 3. We see that the Luneburg lens has a continuum of optical axes passing through the center. It is still difficult to realize in optics (except planar optics as in Jannson & Sochacki, 1980a), with practical applications in microwave antennas.
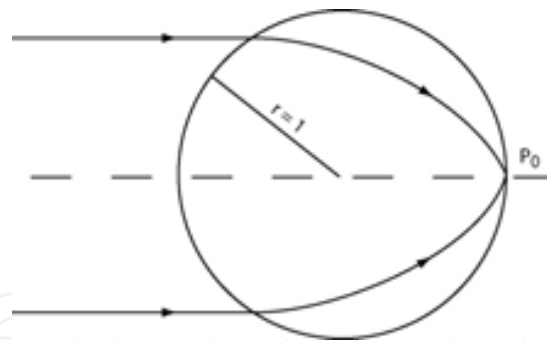
Fig. 3. Illustration of Luneburg lens

2.2 Catadioptric systems

The catadioptric systems are based both on mirrors (catoptric) and lenses (dioptric). They were designed to continue the idea of absolute instruments, such as the Maxwell fish-eye, yet without introducing a GRIN medium. Although they are not absolute instruments, they have an omni-directional view, as shown in Fig. 4, where a parabolic cylindrical mirror is shown. The rays at the bottom are directed to a (refractive) projection lens, where they are imaged at the CCD array. At Physical Optics Corporation (POC), they are applied for periscopic views and video surveillance, where *electronic zoom* is introduced, in particular, and electronic pan, tilt, zoom (PTZ), in general, with a high-resolution cylindrical view, without the necessity of mechanical camera motion.
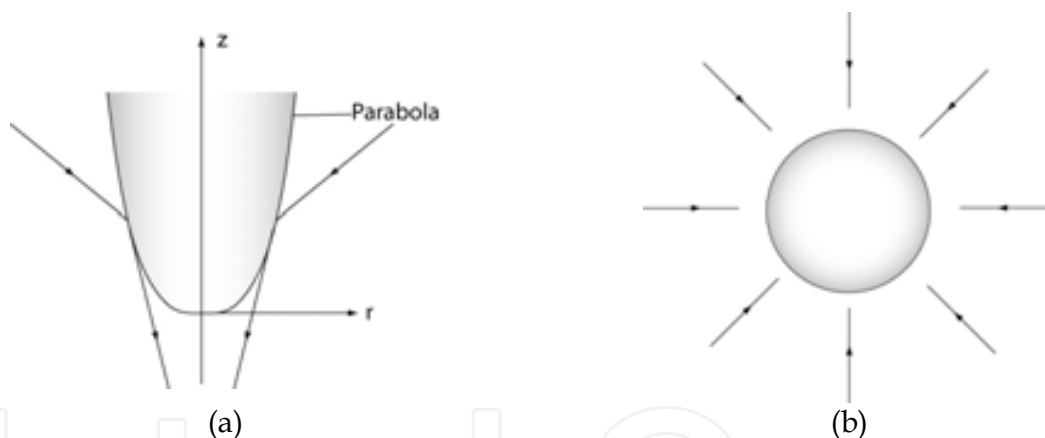

Fig. 4. Illustration of catadioptric system including: (a) Parabolic cylindrical mirror;
(b) Omnidirectional cylindrical top view

Catadioptric systems have panoramic (360°) view; thus, they are similar to Maxwell's "fish-eye." However, they are not GRIN structures. Therefore, calling them "fish-eye" systems (as they sometimes are called in video surveillance applications for panoramic dioptric systems) is a rather unfortunate example of *Artificial Abstraction* (AA), as defined in Section 1.

2.3 Aquatic eyes

In contrast to terrestrial eyes (such as the human eye), when the 1st interface (cornea) has some focusing power due to the difference in refractive indices between air (n_1) and a medium (n_2), the aquatic lenses have zero focusing power for the 1st interface. Therefore, in general, lens focusing is a problem in an aquatic (water) medium. To show this, consider the lens geometry in Fig. 5.
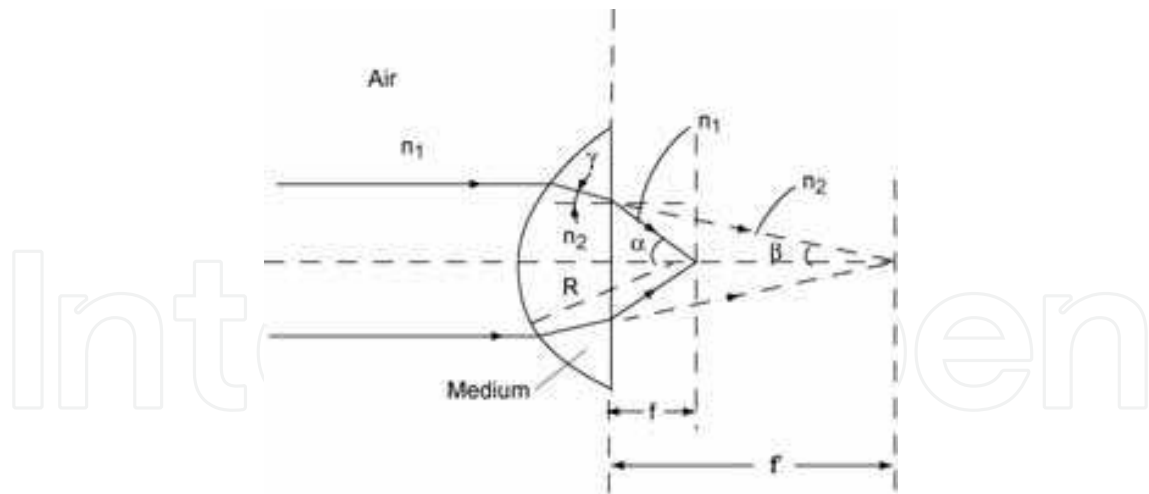
Fig. 5. Lens geometry, illustrating the difference between focusing powers of an aquatic lens (1/f′) and a terrestrial lens (1/f) (here the front interface is the back interface and vice versa). The broken-line ray illustrates an aquatic lens, while the continuous line ray illustrates a terrestrial lens; β = γ

According to Fig. 5, the focusing power of a plano-convex lens (for illustration), 1/f, is (f is focal length),

$$\frac{1}{f} = \left(\frac{n_2}{n_1} - 1\right)\left(\frac{1}{R}\right) = \left(\frac{n_2 - n_1}{n_1}\right)\left(\frac{1}{R}\right) \tag{6}$$

where R is the lens radius of curvature. Using an auxiliary construction from Fig. 5, we obtain: $f\sin\alpha = f′\sin\beta$, for $\alpha, \beta \ll 1$, and from Snell law ($\gamma = \beta$), we obtain $\sin\alpha/\sin\beta = n_2/n_1$; thus the focusing power of aquatic lens, is ($n_1 < n_2$),

$$\frac{1}{f′} = \frac{n_2}{n_1}\left(\frac{1}{f}\right) \tag{7}$$

i.e., n_2/n_1 – times smaller, and substituting Eq. (6) into Eq. (7), we obtain

$$\frac{1}{f′} = \left(\frac{n_2 - n_1}{n_2}\right)\left(\frac{1}{R}\right) \tag{8}$$

Therefore, the axial lens proposition (as in Fig. 5) does not work in an aquatic medium. As a result, Natural Engineering (NE) has selected a GRIN lens such as in Fig. 3, with higher focusing power. A typical aquatic lens, used by fish as well as cephalopods and marine mammals, has f# = 1.25, also known as Matthiessen's ratio (Land & Nilsson, 2002), in memory of Matthiessen's studies in 1880. In Refs. Jagger, 1992 & Nicol, 1989, a comprehensive review of aquatic eyes is provided.

3. A lobster eye as an advanced bug eye system

The surprising discovery of the seeing mechanism of a lobster eye in the 1970s (Vogt, 1980), "allowed shrimp to see," based on reflective optics rather than on more standard refractive optics. Since X-ray refractive optics has always been extremely difficult to achieve, the

lobster eye solution has proven very convenient for (especially) hard X-ray optics. (This section is from Jannson, et al., 2007c.)

Bug-eyes are nonimaging systems with detectors located close to guiding channels. They are called *apposition eyes*, with no transparent (clear) zone allowing for imaging (Fig. 6(a)). In contrast, the **lobster eye** is an imaging system, due to the clear zone between the guiding channels and detector surface (Fig. 6(b)).

The lobster eye has interesting connections with Darwinian evolution. From 1955 to 1975 "shrimps could not see" (i.e., there was no explanation for their seeing mechanism). In 1975, Klaus Vogt, found the solution to this engima (full review in Land & Nilsson, 2002), in the form of two complementary focusing effects: (1) *central ray* one; (2) *skew ray* one. The first is described in Fig. 6(b); the second is based on corner retroreflection, combining two reflections of skew rays, that requires **quadratic** cross-section of the reflection (guiding) channels. Some animals have (1) but do not have (2) (a hexagonal cross-section). All *crustaceans* (shrimp, lobster, crayfish) have both. From an evolutionary point of view, it is interesting that larval stages of some shrimp, have *apposition* eyes, as in Fig. 6(a), with hexagonal facets that change at **metamorphosis** into *superposition* (imaging) eyes, as in Fig. 6(b), with square facets.

(a)   (b)
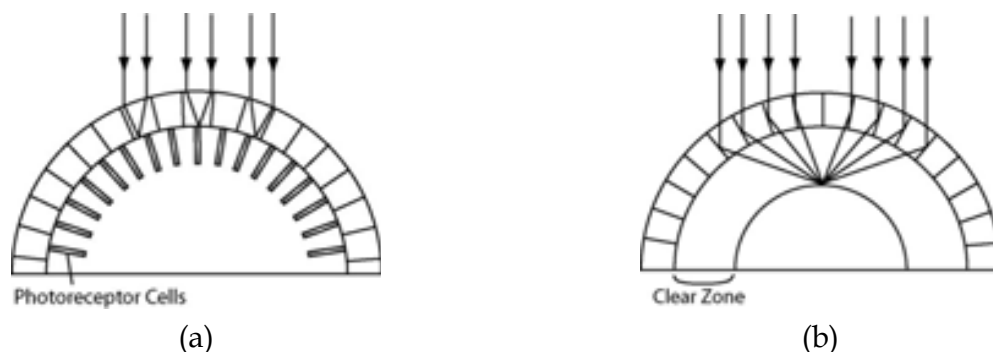
Fig. 6. Lobster eye as advanced bug eye system, including: (a) Bug eye nonimaging system: so-called apposition eye (no transparent (clear) zone); (b) Lobster eye imaging system: so-called superposition eye, with clear zone

The Lobster-eye lens is a transmission lens, based on reflective optics. Typical lenses are based on refractive optics and they are transmission versions. The biological *lobster-eye* lens (LEL) is for visible, or near-infrared (NIR) light, and the reflection channels are filled with material, based on *total internal reflection* (TIR) and Bragg diffraction. POC's LEL, shown in Fig. 7, is for X-rays, and the reflection channels are empty, based on *total external reflection* (TER).

Fig. 7. Illustration of lobster eye, developed at Physical Optics Corporation. The biological lobster eye also has reflection channels with square-cross-sections

The two skew ray reflections from opposite walls of the square-cross-section of a reflection channel (as in Fig. 7) can be formally reduced to a single central reflection, as described in detail in Jannson & Gertsenshteyn, 2006b & Jannson et al., 2007a.
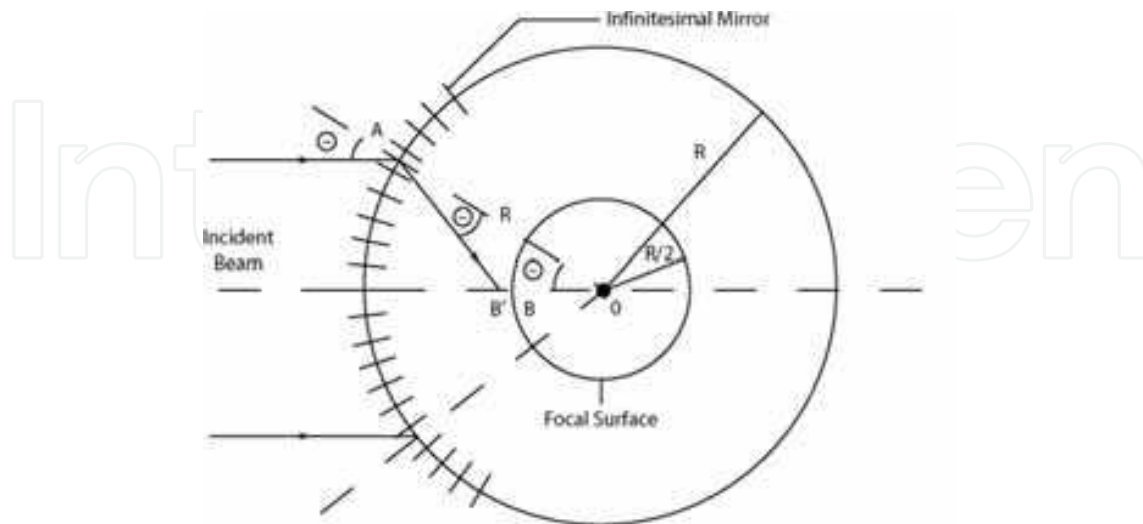

Fig. 8. Lobster-eye lens (LEL) geometry

Assume a continuum of radially directed infinitesimal mirrors located at the circle of radius, R. Then, any parallel (collimated) incident beam will focus at the point (focus), at the sphere of radius, R/2. The LEL geometry is shown in Fig. 8 (above). The essential feature is, that, because of three identical θ-angles, as in Fig. 8, the triangle AB'O has equal legs (AB' = B'O); thus,

$$AB' = B'O = \frac{R}{2cos\theta} \tag{9}$$

Since, for $\theta \ll 1$ (paraxial approximation), we have:

$$B'O = BO \cong R/2 = f \tag{10a}$$

thus,

$$B' \rightarrow B \tag{10b}$$

and, the LEL system is indeed an imaging one. The lens equation has the form

$$\frac{1}{x} - \frac{1}{y} = -\frac{2}{R} = -\frac{1}{f}; \qquad f = R/2 \quad , \tag{11}$$

and the effective aperture radius, a, is equal to $x\theta_c$, for $f = \infty$ where x, y are distances from an object to lens and image to lens, respectively; f is focal length, and θ_c is TER the critical angle (Gertsenshteyn et al., 2005; Jannson et al., 2007a & Gertsenshteyn et al., 2007); thus, it depends on image geometry. Eq. (11) is illustrated in Fig. 9.

From Eq. (11), we obtain the large x-distance of an object, and large y-distance of an image, as shown in Fig. 10. We see that lobster-eye spherical symmetry (Fig. 10) provides realization of the Luneburg lens, without a GRIN medium. In fact, from Eq. (11), for $x = \infty$, $y = f$, thus satisfying the Luneburg lens property of the focusing of any collimated beam.

$$\frac{1}{x} - \frac{1}{y} = -\frac{2}{R} = -\frac{1}{f}; \quad f = \frac{R}{2}$$

2a - Effective Aperture

θ_c - Critical (Maximum) Angle (Grazing)

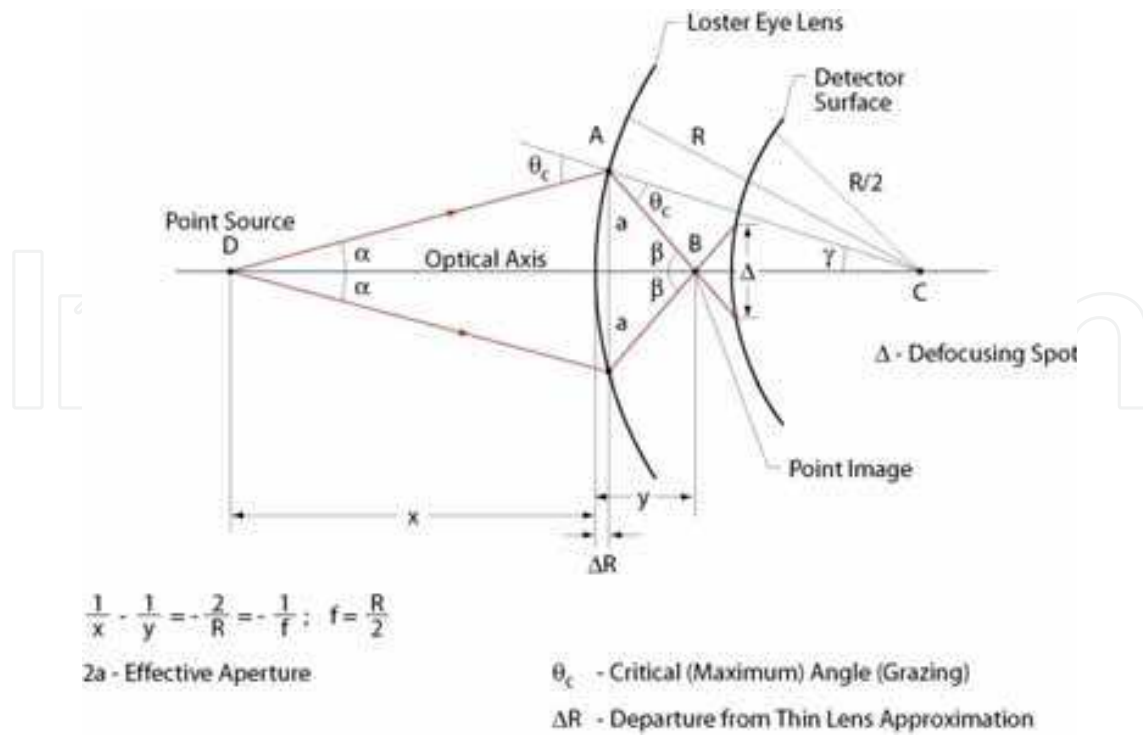ΔR - Departure from Thin Lens Approximation

Fig. 9. Illustration of the LEL Eq. (11), with source point (D) and its image (B)
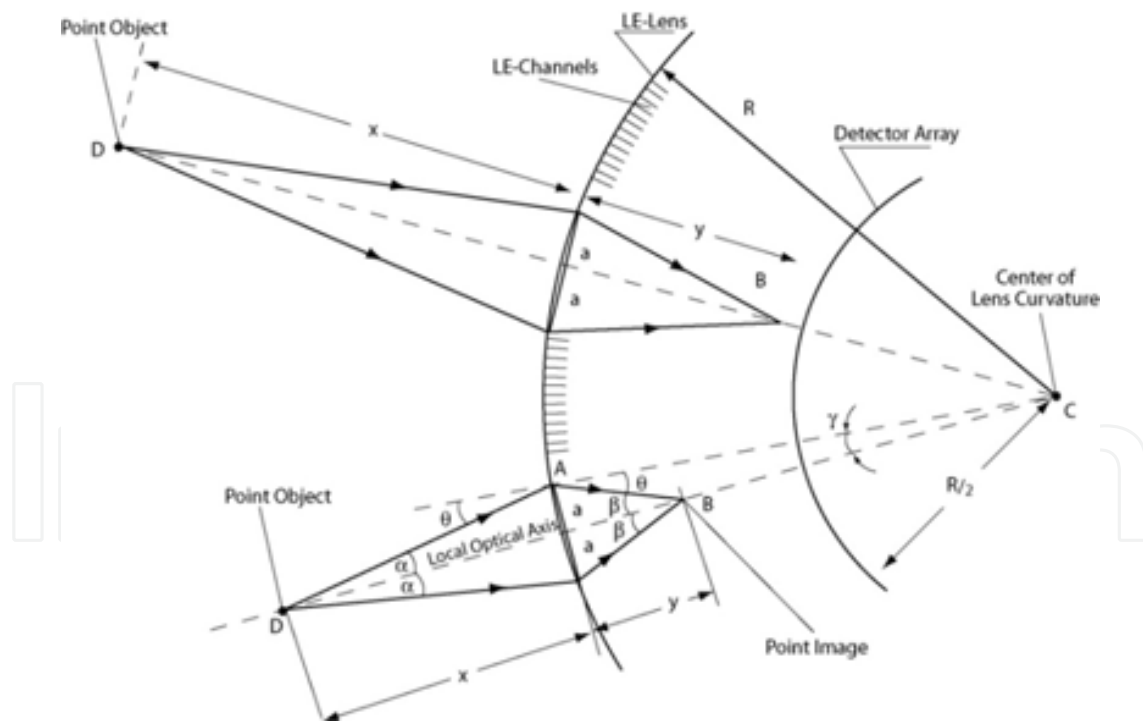

Fig. 10. Lobster-eye spherical symmetry

The ultimate goal of the military is to drop "sensor rocks" that will present a fully hemispheric field of view (FOV), such as bug eyes, or even better a lobster eye (see Fig. 11). The rocks will have natural camouflage, low cost, and disposability, and will work in the visible and IR regions (Grubsky et al., 2006).

Fig. 11. Camouflaged hemispheric lobster-eye awareness sensor, including: (1) IR target; (2), (3), (4), (7) lobster eyes; (5) remote solar panel that can be charged all day to provide electrical energy for all-night operation (in the stationary case); (6) power cable; (8), (12) local solar batteries; (9) metallic waveguide; (10) focal plane array (FPA); (11) sensor housing; (13), (14) sensor "rocks" dropped from the air

4. RGB artificial color vision and biological analogies

4.1 Prior art hyperspectral vs. RGB hyperspectral

The challenge is to combine the two essential features of hyperspectral cameras that are applicable to omnidirectional optical imaging: real-time or *ultrareal-time* (URT) operation, and effective hyperspectral imaging. *Real time* (RT) means 30 frames per second (fps), and *hyperspectral* means over 100 spectral channels (or *bins*) for each pixel during each frame time. This is related to the visible (and NIR), MIR (3-5 μm), or FIR (8-14 μm) spectral region. This is indeed a challenge, because "hyper" means a large number of spectral channels (N>100), and the more spectral channels, the fewer the photons that are available for each detection; so the sensitivity of classical hyperspectral cameras is low. On the other hand, if time-sequential *electro-optic* (EO) filters are used, the hyperspectral camera (Hyvarinen et al., 1998) is slow, far from RT operation. Therefore, in general, "high-speed cameras" and prior art "hyperspectral cameras" perform incompatible operations (this section is from Jannson et al., 2007c).

This dilemma is resolved by introducing the **RGB hyperspectral** camera, based on the novel "RGB vector" concept. In this concept, instead of N > 100 we have N = 2, 3, 4,….12, but, instead of **orthogonal** wavelength channels (as in the case of the classical hyperspectral camera), we have spectral *discriminants*, similar to "color pixels" in a CCD camera, or to color receptors (rods and cones) in the human retina. The novelty is in generalizing this concept to the IR region. The color pixel concept has recently been applied for digital video processing (Kostrzewski et al., 2001 & Jannson & Kostrzewski, 2006a). J. Caulfield is the inventor of the general concept of artificial color (Caulfield et al., 2004).

4.2 Design of color discriminants

The **color discriminants**, or color *primaries*, can be designed for specific object signatures. Those discriminants should discriminate *true targets* from *false targets* even when they have similar wavelength characteristics. Assume for a simplified example that we have five objects of interest: green pepper, snow peas, and carrots, as well as the plate and tablecloth, and that the true target is the green pepper and the remaining objects are false targets. We see that color discriminants can easily eliminate the carrot (orange), the plate (blue), and the tablecloth (white), but both the pepper and snow peas are green, so it is difficult to discriminate between them, so we need a further discriminant, increasing their number from N = 3 to N = 4. This illustrates the principle of how to discriminate targets of interest.

In the case of a **color signature**, or more generally, a *spectral signature*, we apply the generalization of the standard RGB (*red-green-blue*) scheme, represented in VGA video by 24 bpp (8 bpp per color). The RGB scheme can be generalized into similar multicolor schemes for IR (infrared) *multispectral* and *hyperspectral* sensors. Then, instead of comparing sample wavelength spectra with reference wavelength spectra, we compare the generalized RGB color components, which are defined in such a way that they accurately describe the sample *spectra of interest* (SOI). Then, **pixel-to-pixel intensity subtraction** (PIS) in the form of *Euclidean distance*, can be applied to the *color matching operation* (CMO) in the form of *3D pixel vectors*, similar to *speed pixel vectors*, as in *vector flow* analysis. *The color intensity ratio defines the vector direction, while the overall "white" intensity defines the vector module, or value.* Then the CMO is formalized by *color unit vector* (CUV) subtraction.

Let us consider the RGB intensity pixel vector $\vec{I}_{ij}$ (R_{ij}, G_{ij}, B_{ij}), where R_{ij}, G_{ij}, B_{ij} are red, green, and blue RGB color vector components in the form:

$$R_{ij}^2 + G_{ij}^2 + B_{ij}^2 = I_{ij}^2 , \tag{12}$$

where R_{ij} is the ij-th pixel intensity for the red RGB component, and the same for the green and blue components, and

$$\left| I_{ij} \right| = \sqrt{R_{ij}^2 + G_{ij}^2 + B_{ij}^2} \tag{13}$$

is the overall intensity vector module. Thus, the CUV is

$$\vec{U}_{ij} = \frac{\vec{I}_{ij}}{\left| I_{ij} \right|} = \frac{\left(R_{ij}, G_{ij}, B_{ij} \right)}{\sqrt{R_{ij}^2 + G_{ij}^2 + B_{ij}^2}} , \tag{14}$$

and $\left| \vec{U}_{ij} \right| = 1$. CUV subtraction is illustrated in Fig. 12, where $\vec{u}_{ij}$ is a **sample** CUV and $\vec{U}_{ij}$ is a **reference** CUV. This subtraction is in the form:

$$|\vec{\mathbf{u}}_{ij} - \vec{\mathbf{U}}_{ij}| = |\sqrt{(\mathbf{r'}_{ij} - \mathbf{R'}_{ij})^2 + (\mathbf{g'}_{ij} - \mathbf{G'}_{ij})^2 + (\mathbf{b'}_{ij} - \mathbf{B'}_{ij})^2} , \quad (15)$$

where the lower case u, r, g, and b denote the *sample* unit vector $\vec{\mathbf{u}}_{ij}$, while capital U, R, G, and B denote the *reference* unit vector U_{ij} (primes denote **unit** vector components).
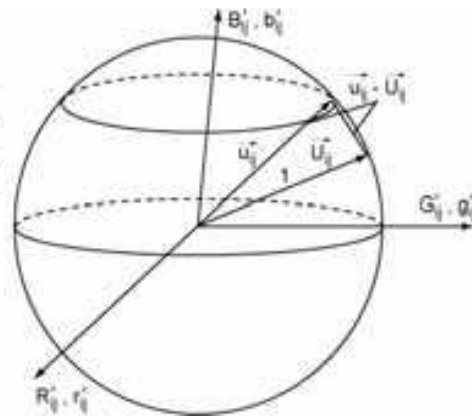

Fig. 12. Illustration of two color unit vector (CUV) subtraction, where $\vec{u}_{ij}$ is a sample unit vector, and $\vec{U}_{ij}$ is a reference unit vector. Cartesian coordinates are unit vector components $\mathbf{R'}_{ij}, \mathbf{G'}_{ij},$ **and** $\mathbf{B'}_{ij}$ for the reference unit vector, and $\mathbf{r'}_{ij}, \mathbf{g'}_{ij},$ **and** $\mathbf{b'}_{ij}$ for the sample unit vector, where: $\left| \overline{U_{ij}} \right| = \left| u_{ij} \right| = \mathbf{1}$. Primes denote unit vector components

The **pixel-by-pixel** vector subtraction operation described above can consume computation time and bandwidth; thus, it is more useful for *automatic target recognition* (ATR). For that purpose we select those pixels for which the CUV subtraction value is below a threshold value, in the form:

$$\left| \overline{U_{ij}} - \vec{u}_i \right| \le \mathbf{T} , \quad (16)$$

where T is a predefined threshold value. The *spectral region* of *interest* (ROI) is defined by those pixel clusters that predominantly have CUV subtraction values below threshold value T. When the color signature has a dominant color component such as red, we can simplify this operation by applying the principle of "bright points," or **bright pixels**. Then, instead of Eq. (16), we can use the following relation:

$$\mathbf{R}_{ij} > \mathbf{T}_B , \quad (17)$$

where $\mathbf{R}_{ij}$ is the absolute color intensity vector $\vec{\mathbf{I}}_{ij}$ component, and the same for green and blue. Then only "red-bright" pixels, which have a value higher than the predetermined threshold value T_B, will be selected. Then the T_B value must be normalized to an average color value to eliminate illumination background. The three RGB color primaries are shown in Fig. 13.

Procedure for finding color primaries in IR. They must be selected in such a way that all wavelength signatures of interest are within the color triangle. Also, to discriminate the specific region well, we need to place two primaries close to each other (for example, the x and y primaries in the 550-650 nm range are well discriminated). Also, some primaries should be expanded into all regions of interest, as the x primary is in the 400-680 nm range, as shown in Fig. 13.
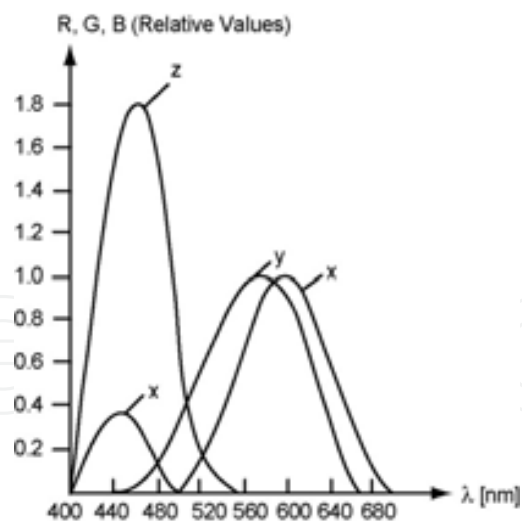
Fig. 13. Illustration of three RGB color primaries in wavelength domain, for human vision. We see that the x-primary is expanded into two hills, covering all regions of interest

4.3 Biological analogies

While human males almost always have three (RGB) color primaries, some women have four (Fu et al., 2004; Caufield et al., 2004 & Fu et al., 2005). Among animals, the *European starling* has four primaries. Other examples include the *mantis shrimp* (twelve primaries! Marshall & Oberwinkler, 1999), *honey bee* (three), and *bichromatic insects* (two). Furthermore, some women not only have four primaries, but also have rod sensitivity even in daylight.

All these biological analogies suggest that the number N of primaries and their related spectral profiles depend on specific tasks or CONOPS. In fact, N varies from two (bichromatic insect) to twelve (mantis shrimp). A specific spectral region of interest should be covered by a higher density of primaries, and the system sensitivity depends on their first differentiating wavelengths. Physically, the color primaries can be created by any of three methods:

- Dichroic beamsplitters
- Detector focal plane arrays (FPAs)
- Color filters directly on the pixels.

4.4 An example of natural engineering

An interesting example of *Natural Engineering* (NE) for aquatic vision is presented in Kröger et al., 1999 for shallow-water fish that have very good color vision, covering 250 nm range from UV to red (four cone types), while still preserving excellent resolution in this wide spectral range in spite of chromatic aberrations (shorter focal lengths for blue). This is due to chromatic aberration compensation by spherical aberration (shorter focal lengths for the inner zone). Then, red light from the inner zone focuses in the same location as the blue light from the outer zone.

5. Resolution and sensitivity in animal eyes

5.1 Resolution

Diffraction-limited imaging systems are those that achieve resolution limits, defined by diffraction rather than by (geometrical) aberrations. Such systems used to have

photoreceptor ("pixel") sizes close to those limited by the *Rayleigh resolution criterion,* based on an Airy (intensity) pattern, in the form: $y = [2J_1(z)/z]^2$, where $J_1(z)$ is the *Bessel function* of the 1st kind and the 1st order, and

$$z = \pi D(\delta\Theta)/\lambda \quad (18)$$

where $\delta\Theta$ is the angular distance from the center of the Airy pattern (which is the point object response), D is the lens diameter, and λ is the optical wavelength (in air). The spatial distance, x, at focal plane, is

$$x = f(\delta\Theta) = \frac{z\lambda f}{\pi D} = \frac{z\lambda}{\pi} f\# \quad (19)$$

where $f\# = f/D$. The Airy (circular) pattern is the diffraction one, with adjacent maxima and minima (rings), defined by the Bessel function, summarized in Table 1, for $\lambda = 0.5$ μm, and $f\# = 2.5$ (easy lens).

Maximum/Minimum	z	x	y
1st maximum	0	0	1
1st minimum (1st ring)	1.22 π	1.52 μm	0
2nd maximum	1.635 π	2 μm	0.0175
2nd minimum(2nd ring)	2.233 π	2.79 μm	0

Table 1. Maxima and Minima of Airy Pattern (Analog Resolution), for $\lambda = 0.5$ μm and $f\# = 2.5$

We see that, outside the 1st ring, the *Airy pattern* is almost flat, close to zero, since for the 2nd maximum, the y value is very low (only 0.0175). The energy fraction within the 1st ring is 84% (Born & Wolf, 1999).

The Rayleigh criterion, defining the analog resolution (valid also for animal eyes) is such that adjacent point objects are recognizable if the 1st maximum of the Airy pattern of the 1st object coincides with the first minimum of the 2nd one. According to Table 1, this is equivalent to $z = 1.22\pi$; thus, we obtain the following resolving angular element, $(\delta\Theta)^R$,

$$(\delta\Theta)^R = 1.22 \, (\lambda/D) \quad (20)$$

and, the equivalent linear element $(\delta x)^R$, in the form:

$$(\delta x)^R = 1.22 \, \lambda f\# \quad (21)$$

In contrast, the digital resolution (valid for *Human Engineering* (HE)), is defined by the so-called *Nyquist Criterion,* which states that two point objects are recognizable if they are located not closer that at the distance between two second pixels. Assuming, for illustration, that the size of each pixel is 4 μm, and the space between them is 1 μm, the *pitch* is 5 μm and the Nyquist resolving element, $(\delta x)^N = 10$ μm, as shown in Fig. 14, where the Rayleigh resolving element: $(\delta x)^R = 1.52$ μm, is also shown, for $\lambda = 0.5$ μm, and $f\# = 2.5$.

The Nyquist criterion can also be applied to *Natural Engineering* (NE), if we identify the eye's photoreceptor size with pixel size. The HE-based video surveillance also uses the 3rd
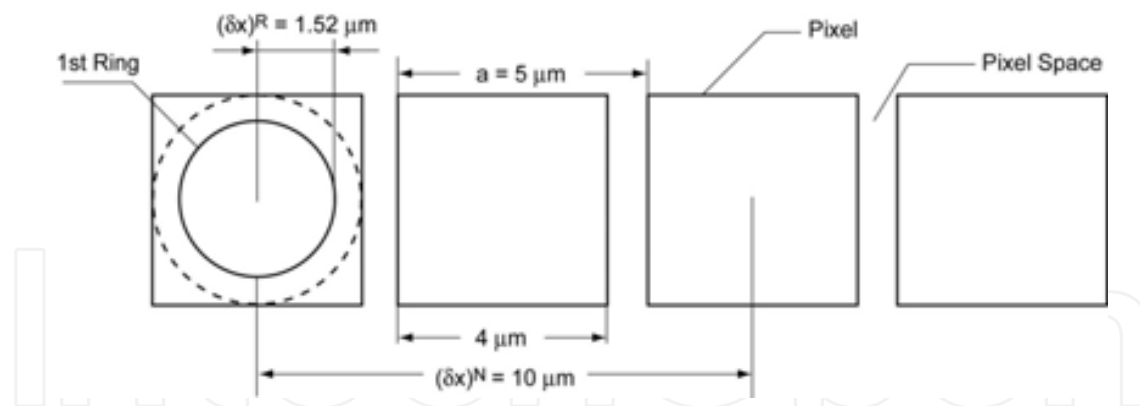
Fig. 14. Illustration of digital (Nyquist) resolution ($\delta x^{(N)} = 10$ μm), and analog (Rayleigh) resolution ($\delta x^{(R)} = 1.52$ μm)

resolution criterion, the so-called *Johnson criterion*, defined as a minimum number of pixels per object for: *detection* (D), *recognition* (R), and *identification* (I), as: 5, 10, and 15, respectively. For example, for an object (human) with a size of 1.8 m, the Johnson resolving elements are: 36 cm (D), 18 cm (R), and 12 cm (I), respectively.

Resolving Elements and Spatial Frequencies. In order to explain the role of the resolving element in animal eyes' resolution, consider the object detail, $\delta\ell$, to be observed at distance, r; then its angular size is $\delta\phi = \delta\ell/r$, and, assuming imaging system magnification, M = 1, the angular size of the image of this object detail, is also $\delta\phi$ (for, M ≠ 1, we need to provide respective rescaling). The Rayleigh criterion defined by Eq. 20, determines the minimum recognizable angular size of such a detail.

The other important resolution quantity is *spatial frequency*, defined in Fourier optics (Goodman, 1968), by the so-called *Fourier transform* of 2D function U(x,y):

$$G(f_x, f_y) = \hat{F}\{U(x,y)\} = \int_{-\infty}^{+\infty} \int U(x,y) \exp\left[-j2\pi(f_x \cdot x + f_y \cdot y)\right] dxdy \qquad (22)$$

where $\hat{F}\{...\}$ is the 2D Fourier transform of U(x,y) and (f_x, f_y) are 2D-spatial frequencies in the number of lines per mm. For example, for $f_x = 100\ell/mm$, the resolving element (spatial period) is: 10 μm = 10^{-2} mm.

In Land & Nilsson, 2002, spatial frequency is defined in a different way, namely, in a number of cycles per radian, as the *optical cut-off frequency*, ν_c, in the form:

$$\nu_c = D/\lambda \qquad (23)$$

It can be shown that the equivalent Fourier cut-off frequency, f_c, is equal to $D/\lambda f$, for far-distant objects (see Goodman, 1968), *Frequency Analysis of Optical Imaging Systems*, for $d_i = f$), where the *Optical Transfer Function* (OTF) for noncoherent optical imaging systems reaches zero. This is equivalent to contrast ratio reaching zero for cut-off "spatial frequency," $\nu_c = D/\lambda$, Fig. 3-3, in Land & Nilsson, 2002.

The cut-off spatial frequency ν_c, as defined in Land & Nilsson, 2002, is a useful quantity in such a way that, according to Eq. (20), we have:

$$\nu_c = 0.82 \, [(\delta\Theta)^R]^{-1} \qquad (24)$$

i.e., it is approximately equal to the minimum recognizable angular object size, seeing at λ wavelength, with lens aperture diameter, D. The typical color wavelengths are: *red* (600-640 nm), *yellow* (570-600 nm), *green* (510-570 nm), and *blue* (450-510 nm). According to Schever & Kolb, 1987, the more subtle subcolors are: violet region (320-420 nm); blue region (420-500 nm); green-yellow region (520-580 nm); and orange-red region (590-610 nm). On the other hand, the mantis shrimp (*Neogonodactylus oerstedii*), a marine crustacean, has at least four color stimuli for UV light, at 315, 330, 340, and 380 nm (Marshall & Oberwinkler, 1999). Assuming D = 2 mm, and λ = 0.55 μm = 550 nm), we obtain v_c = 3637 cycles/radian. According to Land & Nilsson, 2002, the highest v_c value is 8022 cycles/radian for an *eagle*; a *man* (fovea) is *second* with v_c = 4175 cycles/radian; then, the *octopus* (2632) and *jumping spider* (716); then, the *cat* (573), *goldfish* (409), and *dragonfly* (115); finally, with much lower resolution: *bee* (30), *crab* (19), *scallop* (18), *fly* (5.7), *nautilus* (*cephalopod:* 3.6), and *cirolane* (deep-sea *isopod:* 1.9).

The spatial visual *acuity* of the wedge-tailed eagle (*Aquila audex* (Raymond, 1985)) has been determined across a range of luminance, by applying behavioural (acuity) and anatomical (resolution) investigation (the eagle viewed test gratings and received a food reward if his grating resolution guess was right). The results were average acuity: from 138 c/deg (or, 7911 c/rad), for luminance of 2000 cd/m^2, to 34 c/deg (or 1948 c/rad), for luminance of 0.2 cd/m^2, corresponding to almost the same values of resolving power.

5.2 Sensitivity

Eye sensitivity is defined as the number of photons, N, received by a photoreceptor, with size, d, by a lens with an aperture diameter D, and a focal length, f, at a standard radiance (luminance) level, in the form (Land & Nilsson, 2002):

$$S = N / R = 0.62 \, (d^2 / f\#^2) \, (\eta_{abs}) \qquad (25)$$

where radiance, R, is in Watts/sr·m^2 (*objective* units), while luminance is in (cd/m^2, or nits (*subjective* units), f# = f/D, and η_{abs} is coefficient (fraction) of absorption. We see that *aquatic eyes* with very low f#-values are preferable here, while maximizing d-value (pixel size) also minimizes resolution. Of course, at very high luminance level, S-value can be low, but at very low ones, S-value should be high.

In Table 2, various luminance levels are presented, as summarized from various sources, especially including Land & Nilsson, 2002. We see that their range is very broad, from 10^{-8} nits (800 m – water depth), or even lower, to 10^4 nits (bright sunlight). At water depth, ℓ, the radiance (luminance) attenuates exponentially (according to Beer's law), as: $R = R_o e^{-\alpha \ell}$, where α = 0.032 m^{-1}.

Eye sensitivities are adjusted to specific light *habitat*. For example, for human light in daylight, s = 0.01 μm^2 sr (D = 2 mm, (d/f) = 1.2·10^{-4} rad, and η_{abs} = 0.31; so, for d = 2.5 μm, we obtain f = 20.83 mm), while for the deep-sea *isopod* (*Crustacean Cirolana*), s = 4200 μm^2 sr (D = 150 μm, (d/f) = 0.78 rad, η_{abs} = 0.51; so, for f# = 1, f = D = 150 μm, and d = 117 μm; i.e., large size of photoreceptor).

Typical sensitivity levels for animal eyes are decreased with higher luminance levels (Land & Nilsson, 2002): *Cirolana* (marine *isopod* at deep sea): s = 4200 μm^2 sr; *Oplophorus* (*decapod* shrimp at deep sea): s = 3300 μm^2 sr; *Dinopis* (ogre-faced spider, nocturnal): s = 101 μm^2 sr; Moth *(nocturnal)* s = 38 μm^2 sr; *Man* (scotopic): s = 18 μm^2 sr; *Scallop* (coastal sea-floor):): s =

*) Arrows show Luminance level in Nits [cd/m²], corresponding to specific Luminance condition.
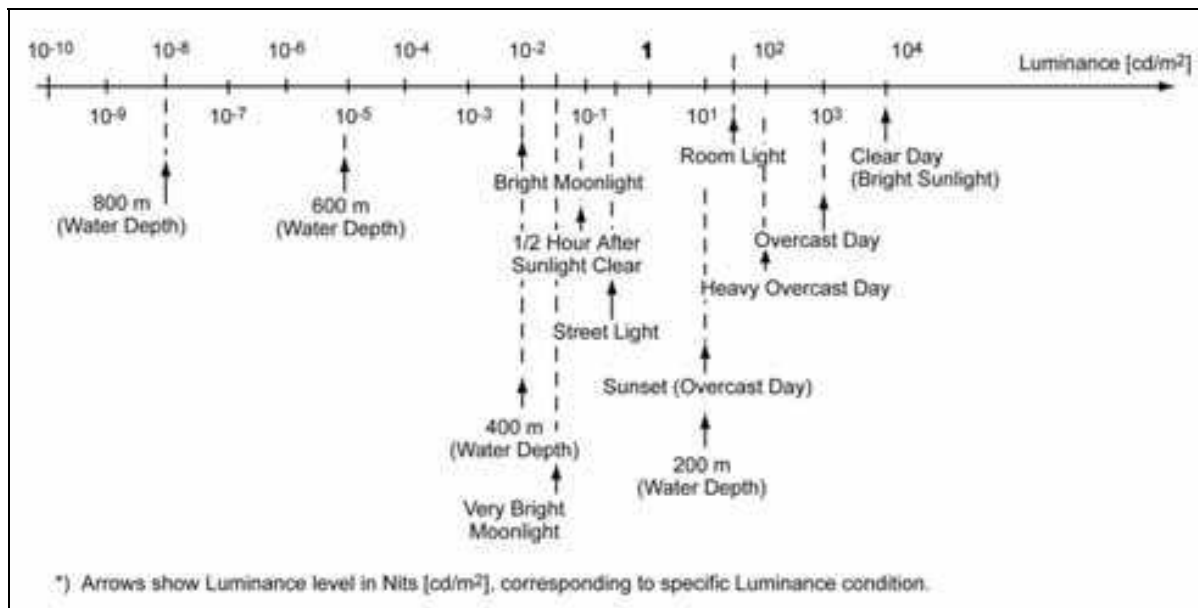
Table 2. Luminance Levels[*)]

4 μm² sr; *Crab* (diurnal):): s = 0.5 μm² sr; *Bee* (diurnal):): s = 0.32 μm² sr; *Jumping spider* (diurnal): s = 0.04 μm² sr; and Man (*fovea* in daylight):): s = 0.01 μm² sr.

5.3 Contrast and low photon numbers

Human eyes, as well as the majority of mammal eyes, have excellent sensitivity to low photon levels, even to single photons (Land and Nilsson, 2002), although the brain's "safety factor" (an equivalent of "decision threshold" in HE-photodetectors) is of about: N = 6. For such low photon numbers, N, the *quantum noise* occurs, guided by *Poisson statistics* (Margenau and Murphy, 1976). Its basic feature is such that the photon beam with statistical average, $\bar{N}$, fluctuates with dispersion, $\sqrt{N}$ (these fluctuations are of fundamental quantum nature, independent on measurement accuracy). This means that low contrast ratio levels (defined as light intensity relative variation: $C = \Delta I / 2I$, where $\Delta I = I_{max} - I_{min}$) cannot be kept at low photon numbers. (The contrast is an important parameter of vision measuring "*spatial edges*" and "*object contours,*" or even "*temporal contours.*") Assuming $\Delta I = 2\sigma$, where σ is dispersion, we obtain

$$C = \frac{\Delta I}{2I} = \frac{\sigma}{I} = \frac{\sqrt{N}}{N} = \frac{1}{\sqrt{N}} \tag{26}$$

which is a generalized form of the so-called *Rose-deVries law*, studied by Hugo deVries and Albert Rose in the 1940s (Land and Nilsson, 2002).

This law shows that low contrast ratios, C, can be measured only at high photon levels. For example, for N = 10,000 = 10⁴, $\sqrt{N} = 100$, and C = 1%. However, for N = 100, $\sqrt{N} = 10$, and C = 10%. In general, there is the rule that for nocturnal vision (equivalent to night vision in Human Engineering (HE)), we need to have animal eyes with high sensitivity (thus, with low resolution), in order to measure low contrast levels. This is the manifestation of general trade-offs between high *metrical information* capacity (or, high dynamic range and low contrast) and *high structural information* capacity (or, high resolution) (Jannson, 1980b and MacKay, 1950); simply speaking, we cannot have low contrast detectivity and high

resolution at the same time, when photon levels are low. This general law is valid for any type of measurement noise, not only quantum noise.

To be complete, let us also discuss the so-called specific detectivity, or $D^* = \sqrt{AB}\ /(NEP)$, valid for HE-semi-conductor photodetectors, where A-detector surface, B-bandwidth, and NEP-equivalent noise power, in: $W^{-1}cm\ Hz^{1/2}$. Good D*-values are in the range of $10^{12} - 10^{13}$ $W^{-1}cm\ Hz^{1/2}$.

Let us consider the human eye with decision-threshold: N = 6 (against spontaneous *rhodopsin* activations (Land & Nilsson, 2002)). From X-Ray Data, 2001, we have: hc/1 eV = 1.2 μm, where h-Planck constant, c-speed of light; thus, hν = hc/λ = 1 eV, for λ = 1.24 μm, or hν = 2 eV, for λ = 0.62 μm (ν-photon frequency). Then, for λ = 0.62 μm, (red), (NEP) = (6) $(3.2)\cdot10^{-17}$ J/sec = $19.2\cdot10^{-17}$ W, assuming noise level (floor) for N = 6 during 1 sec-observation. Assuming retina's "pixel's size: $d = \sqrt{A} = 2.5\ \mu m$, we obtain: D* = ($2.5\cdot10^{-4}$ cm) (1 $Hz^{1/2}$/($19.2\cdot10^{-17}$ W) = $1.3\cdot10^{13}$ $W^{-1}cmHz^{1/2}$; i.e., an excellent D*-value.

For (noise) fluctuation, based on Poisson statistics (or, in general, on Gaussian (normal) statistics) (Margenau & Murphy, 1976), it is useful to evaluate light-intensity variations in dispersion (σ) units. Then, we can easily determine probability, p, that a given N-value is located within the range: $N = \bar{N} \pm \varepsilon\sigma$, where ε is a number of σ-units, as shown in Table 3, based on the so-called *normal probability integral* (Dwight, 1961), related to *error-function*, tabulated in other sources.

ε	1.0	1.5	2.0	2.5	3.0	3.5	3.8
p	68.3%	86.6%	95%	98.8%	99.7%	99.35%	99.99%

Table 3. Probability P, of N-Number Location within: $N = \bar{N} \pm \varepsilon\sigma$, based on Normal Probability Integral

6. Animal mirrors and other natural optical elements

Animal mirrors cannot be **metallic** but rather **dielectric** ones. In such a case it is quite surprising that such a complex effect like *Bragg effect* has been discovered by the NE, including even *tunable interference filters* performing color changes in reflection (Lythgoe & Shand, 1989). This is because by changing the spatial period, Λ, due to mechanical shrinking effect, we can change resonant (Bragg) wavelength, $λ_B$, by the following Bragg resonance relation:

$$\Lambda = \frac{\lambda_B}{2\bar{n}} \tag{27}$$

where $\bar{n}$ is average refractive index, as shown in Fig. 15.

According to the *Bragg triangle* (Fig. 15(b)), we have: K/2k=cosα′, or λ′ = 2Λ cosα′; sinα = $\bar{n}$ sinα′, the latter equation to be Snell law, while λ′ = λ/$\bar{n}$ (where λ′ is in medium while λ is in air), and using Eq. (27), we obtain the following "blue-shift" relation (K = 2π/Λ, k = 2π/λ′):

$$\lambda' = \lambda_B \cos\alpha'; \tag{28}$$

i.e., **Bragg wavelength shifts-into-blue** under slanted (α′>o) incidence (strictly speaking, any wavelength value and corresponding Bragg mirror efficiency value will be shifted under slanted incidence, according to Eq. (28)). This effect provides a good criterion for
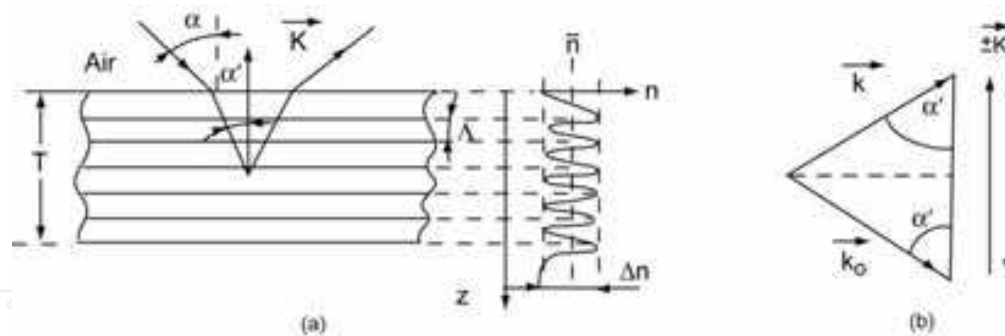
Fig. 15. Illustration of Bragg effect in sinusoidal Bragg grating, including: (a) Bragg reflection; (b) Bragg triangle

differentiation between metallic mirrors and Bragg mirrors. Still, the majority of *butterfly* wings have pigmentary (similar to metallic) mirrors. However, males of the genus *Morpho* have intensive blue wings based on constructive interference (Bragg effect in dielectric mirror).

The structural (Bragg) animal mirrors are based on *sinusoidal* index modulation (as in Fig. 15(a)) rather than on quadratic one, as in the case of HE-interference filters. Therefore, they are closer to *holographic Bragg mirrors*, such as those based on *dichromatic gelatin* (DCG) (Jannson et al., 1991), which is **volume holographic material**, **extracted from biologic tissues.** Then, Kogelnik's coupled-wave theory (Kogelnik, 2001) holds, with *coupling constant*, ν, defined as: $\nu = \pi \Delta n \cdot T / \lambda'$, where Δn is *index modulation* and T-grating thickness, as in Fig. 15(a). For $\nu = \pi$, the holographic (diffraction) efficiency reaches 99%; then, $\Delta n \cdot T / \lambda' = 1$, and required $\Delta n = \lambda / n \cdot T$. At the same time, the *Bragg grating linewidth,* $\Delta \lambda$, is defined by the relation: $\Delta n / \bar{n} = \Delta \lambda / \lambda$, and number of grating periods, M, is: $M = T / \Lambda = 2 \bar{n} T / \lambda$; thus, combining all these relations, we obtain the following relation for Bragg linewidth, $\Delta \lambda$, preserving high (99%) diffraction efficiency,

$$\frac{\Delta \lambda}{\lambda} = \frac{2}{\bar{n} M}; \quad M = \frac{2\lambda}{\bar{n} \Delta \lambda} \tag{29}$$

For example, for $\lambda = 600$ nm, $\Delta \lambda = 10$ nm, and $\bar{n} = 1.45$, we obtain M = 82; and, since: $T = M \lambda / 2 \bar{n}$, we obtain T = 17 μm, a very small mirror thickness (sufficient to obtain such high (99%) reflection). On the other hand, for $\alpha = 30°$ and $\lambda_B = 600$ nm, we obtain from Eq. (28), $\lambda = 563$ nm; i.e., the **blue-shift** is significant (36 nm).

Vignetting has been discussed in Section 1, as a vision effect discovered by the NE-based precursor of an eye (Fig. 1). In fact, such a primitive eye is still applied as *Nautilus* eye. Other *cephalopods* (*octopus*, *squid*, *cuttlefish*) have quite excellent eyes. This surprising NE-bottleneck can be explained by the fact that the Nautilus habitat is rather low risk. (Also, NE-moving into high-resolution small-pupil *pinhole* eyes would be impractical due to too-low sensitivity.)

Anti-Reflection (AR) Structures in the animal world are based on a pigment (like "black paint") material, rather than on the so-called *moth-eye AR-structures*, proposed by the HE, based on cone-like sub-wavelength microscopic structures, simulating GRIN-reflection, as shown in Fig. 16.

In such a case, in the intermediate ("GRIN") region: $0 \le z \le z_o$, the refractive index, n(z), changes as: $n = n_1 w + (1-w) n_2$, where w is a *weight factor:* $0 \le w \le 1$, in the form: $w = z / z_o$, which is illustrated in Fig. 16, for $n_2 = 1$ (air). This approximation is valid only if there is no "diffraction grating" effect, even for very large incidence angles; i.e., when $\Lambda < \lambda / 2$. Since such solution (applied for HE-optical/microwave AR-structures) has not been discovered
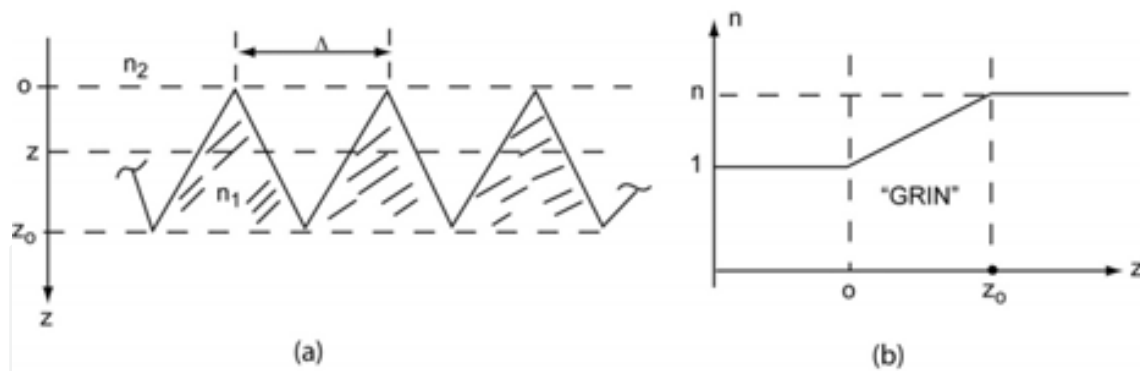
Fig. 16. Illustration of HE-"moth-eye" structure, simulating GRIN effect for $\Lambda < \lambda/2$, assuming $n_2 = 1$ (air), including: (a) Moth-eye AR-structure; (b) GRIN dependence: $n = n(z)$

by the NE, we need to call the "moth-eye" concept, as a kind of *Artificial Abstraction* (AA); see; also, non-Lambertian diffusers (Jannson et al., 2006c).

Total Internal Reflection (TIR) has been discovered by the NE in *superposition* eye of freshwater crayfish, *Cherax destructor*. Cherax is basically nocturnal and has a reflection superposition eye (see Section 3). In Bryceson & McIntyre, 1983, the TIR acceptance angles have been measured and average FOV curves were calculated to be within 5-10°, depending on light habitat. It should be noted that the TIR is much easier to achieve than the Bragg reflection (Fig. 15), as shown in Fig. 17, where the "mirage" phenomenon is also shown (such index profile can also be obtained in hot desert air environment).
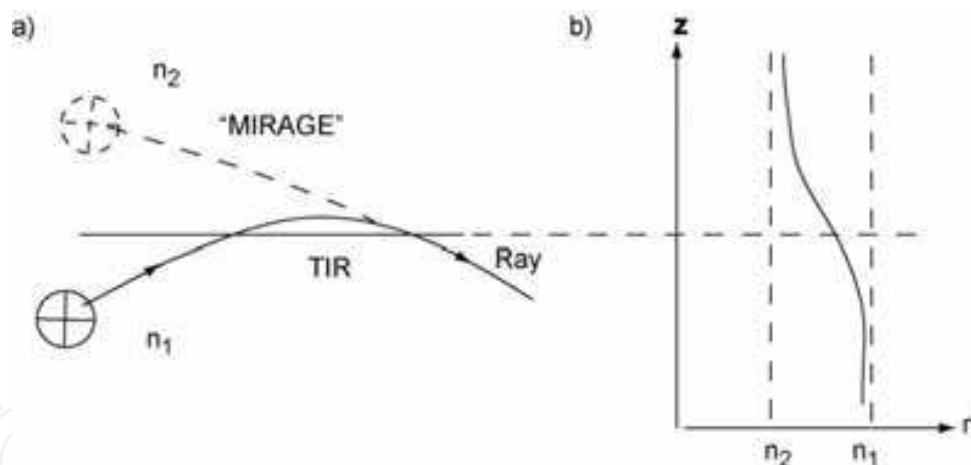

Fig. 17. Illustration of Total Internal Reflection (TIR) effect ("total" means 100%) in animal superposition eye optics; $n_1 > n_2$, including: (a) "curved" ray reflection; (b) index profile

Reflecting Camouflage is applied by some fish such as *permits* (*trachinotus falcatus*). These are silver fish that apply a form of camouflage which in the open ocean makes their bodies very difficult to see (Denton & Nicol, 1965), because direct solar component becomes diffuse below the sea surface; so, the radiation becomes symmetrical around vertical axis. As a result, independently on sun light direction, a vertical mirror surface becomes invisible (light reflected from such a surface at any angle has the same intensity as the light passing through this surface). Therefore, by placing fins vertically (not parallel to the body surface) makes fish almost invisible. This effect works independently on color if the multi-layer (Bragg) mirrors are applied with proper color compensation (please see, Land & Nilsson,

2002, Section 6). It should be noted that a similar CONOPS (to that below sea surface) is under heavy canopy of rain forest.

Scotopic Nocturnal Vision is applied by primates and higher mammals, by applying two types of photoreceptors: *cones* and *rods*. In the case of **photopic** (diurnal) vision (field luminance not lower than 3nt (cdm^{-2})), we apply cones (after being dark adapted, the eye requires 2-3 minutes to become light adapted). In the case of **scotopic** (nocturnal), or night vision (field luminance not higher than $3 \cdot 10^{-5}$nt), we apply rods (dark adaption takes 45 min.). Retina's highest resolution area, *fovea,* contains only cones. The maximum photopic efficiency is at 555-nm wavelength, while the maximum scotopic efficiency is at 510 nm (*blue-shift*). The mixed (photopic/scotopic) light habitat is very frustrating for the human eye. Such habitat can be created, for example, by scattered street light, filling all the intermediate (10^{-5}-1 nt) region (see Table 2). This defect can be eliminated by LED illumination. Also, the change of sunlight spectrum (blue-shift for scotopic) can influence human sleep habit (level of melatonin is increasing in human blood under blue-shift of white light, simulating sunset conditions (Brainard et al., 2001)) which is broken under artificial lighting. This, again, can be regulated by LED illumination.

Infrared (IR) Vision has been applied to the detection of forest fires by the beetle *Melanophila accuminata* for mating purposes which usually takes place while the fire is still burning and females deposit eggs immediately after the flames have subsided (the larvae of Melanophila absolutely depend on wood of fresh fire-killed trees because they cannot cope with the defense reactions of a living tree). Forest fires emit IR radiation at 2.2 - 4 μm (assuming fire temperature between 500°C and 1000°C,) which is well transmitted through air due to atmospheric "window" ranging from 3 μm to 5 μm, at distances up to 80 km. In the experiments (Schmitz & Blackmann, 1998), all wavelengths shorter than 1.6 μm were excluded by a longpass IR filter.

7. Pseudo-apposition eyes

The apposition eyes of insects produce multiplicity of redundant identical images. This redundant imaging information is further lost through neuro-biological process. In this section, we propose a HE-based solution, called *pseudo-apposition eye*, which applies this imaging multiplicity information for spectral imaging purposes, as shown in Fig. 18. This *hyperspectral imaging* concept applies narrow band interference filters located in the front of each lens with different Bragg wavelengths λ_1, λ_2, λ_3, etc., representing different spectral bands. Each lens has its own camera with 2D photoreceptors (pixels). Since this system observes distant objects, at infinity, each so-called *world object point* is represented by certain plane wave with direction in spherical coordinates (Θ, ϕ). While every spectral band is represented, at normal incidence ($\Theta = 0$), by its central (Bragg) wavelength λ_1, λ_2, λ_3, etc., this wavelength is <u>shifted</u> into shorter wavelengths for slanted angle incidence $(\Theta > 0;\ \theta \leq \pi/2)$, due to *Bragg wavelength shifts-into-blue* effect (see; Eq. (28)). Because this system monitors only plane waves, the lenses required have to produce only simple plane-wave-transformation-into-an-image-point, equivalent to Fourier transform, as in Eq. (22). The geometrical locii of these image points can be called an analog of Petzval's surface (Born and Wolf 1999), because this surface does not represent the same wavelength but rather Bragg wavelength distribution following Eq. (28). The optimum lens realizing this surface should be a kind of ball lens, with maximum number of degrees of freedom in order to maximize the optimization process (Kompaniets, 2010). Therefore, the ideal lens should be a
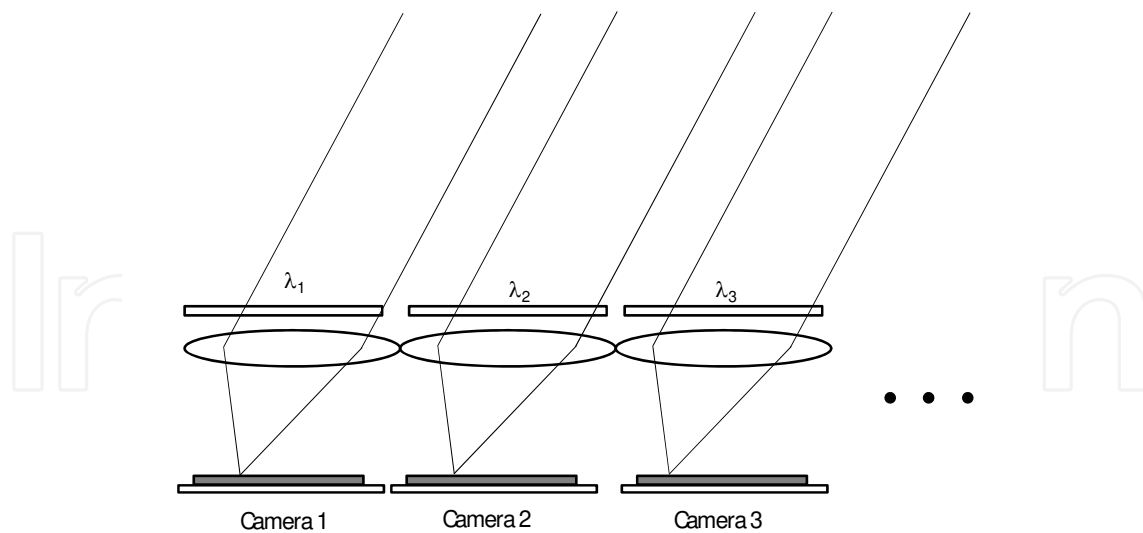
Fig. 18. A possible implementation of the hyperspectral imaging concept based on use of multi-aperture pseudo-apposition eye system. As shown above, multiple cameras observe the same scene at different spectral bands. Position of the object of interest in the so-called RGB color map can be determined by brightness of the relevant pixels in the multiple spectral bands

kind of GRIN lens, similar to that used in aquatic eyes, as in Section 2.3. Fig. 19 shows the photograph of object mapping with traces of TNT explosive (invisible to the naked eye), detected by the pseudo-apposition eye system.
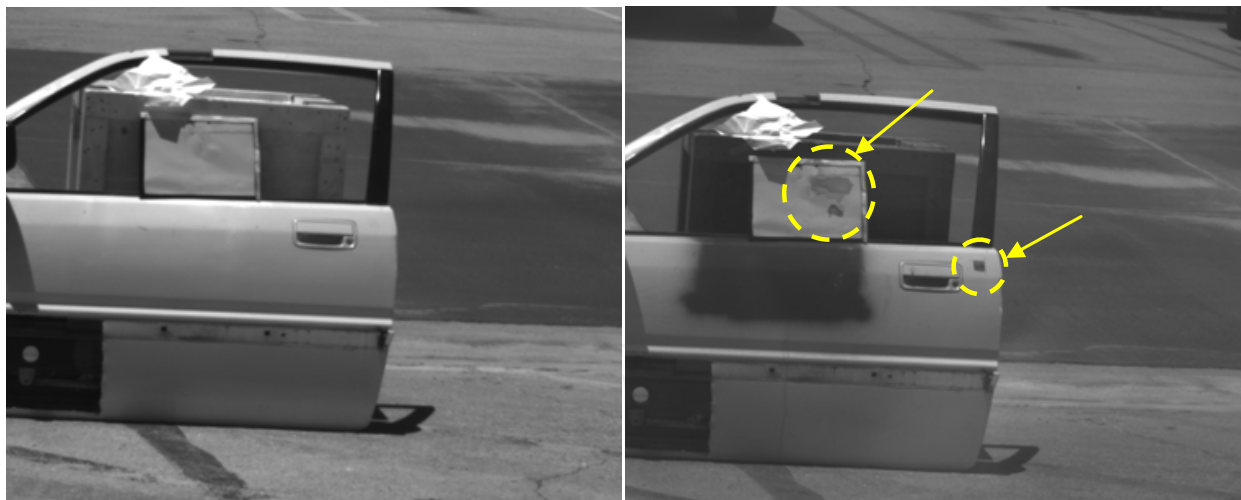

Fig. 19. Left – image captured using a regular monochrome camera that shows no traces of explosives. Right – Dashed yellow circles clearly show traces of explosives made visible through passive spectral imaging

8. Human eye, visual cortex and video imagery effects in primates' vision

8.1 Eye, retina and primary visual cortex
Analyzing human vision (or, more generally, primates' vision), in the context of video imagery, requires considering not only the eye but also the *primary visual cortex*. This, in

turn, requires discussing not only human vision in a narrow sense (i.e., eye, including retina) but also the field of *central-nervous neurobiology*. In this section, we will present highly simplified (broader) view of human vision including NE-based temporal imaging effects related to **HE-based video surveillance**, based on excellent monography by Hubel (Hubel, 1988), a Nobel laureate with Wiesel in 1981). He refers to Ramon y Cajal and Golgi as fathers of *neuroanatomy* (Nobel prize in 1906). In Fig. 20, we show the topography of human brain emphasizing the eyes and primary visual cortex (Fig. 20(a)), including human left eye (Fig. 20 (b)), and microscopic view of eye's retina (Fig. 20(c)).

The **primary visual cortex** is located at the opposite side to the eyes (Fig. 20(a)). The second surprising fact is that the optic nerve bundles are reshuffled at *optic chasm* cross-roads: left-to-right and vice versa, at about 50/50-proportion ratio, while this ratio is different for lower mammals such as horses and mice (for more details, please see Hubel, 1988, Section 4). After passing cross-roads, the optic nerve bundle is distributed into broad so-called *optic radiation* channeling and then converged into a narrower channel leading to *primary visual cortex*.

As an *eye on a land* (terrestrial), the human eye has *cornea*, with some focusing power allowing to make homogeneous axial lens solution effective (in contrast to aquatic GRIN lenses). At the front of the lens there is *iris* (pupil), with its size tunable to various light habitats, while eye's accommodation (equivalent to camera's variable focal length) is provided by eye curvature change due to *ciliary muscles* (while *extraocular muscles* regulate the entire eye ball motion) as in Fig. 20(b). The light beam is focused into *fovea* which is a small part (about half millimeter in diameter) of *retina* (equivalent of CCD array).

Retina's photoreceptors (CCD pixel's equivalents) are both (scotopic) *rods* (which are far more numerous than cones) and (photopic) *cones*, totally about **125 million**, with fovea, a high-resolution spot, containing only cones. Behind photoreceptors, there is a back layer containing the *black pigment*, *melanin* (also found in skin), an equivalent of black paper inside a camera. It has also the second function: restoring functionality of photoreceptors after their bleaching by strong light beams. This is perhaps the reason that retina's thin (250 μm) semi-transparent neural cell structure (Fig. 20(c)) is placed into the front of light; thus, partially scattering (blocking) light beams, resulting in some obscuring of vision. This "*purposely mistaken*" NE-solution seems to be necessary compromise between eye optics and melanin's biochemical functionality needs. [Cones and rods, with 2-3 μm-diameter size, are terminated with "pixels;" their size is close to the diffraction (Rayleigh resolution) limit (~1.5 μm).] The light blurring, due to this compromise, would be disastrous in the fovea region, when high resolution demands are very stringent; thus, the NE provided a ring of thicker retina exposing the central cones of the fovea region, thus, avoiding its blocking (Hubel, 1988).

In Fig. 20(c), three retinal layers: *ganglion cells*, *bipolar cells* and rods/cones are shown; their total thickness is only 0.25 mm = 250 μm. We see that light needs to pass through two of them (ganglion and bipolar) before it gets to the rods and cones. Since the number of cells increases from left to right (from about 1 million to 125 million), two other in-parallel cells (*horizontal* and *amacrine* ones) provide the necessary fan-out.

Considering photoreceptor size of about 2.5 μm, and total number of cones/rods to be about 10^8, the retina size is about 25 mm, with semi-circular surface profile (Fig. 20(b)), to be reduced to about: 25 mm/$(\pi/2)$ = 16 mm of straight-line length.
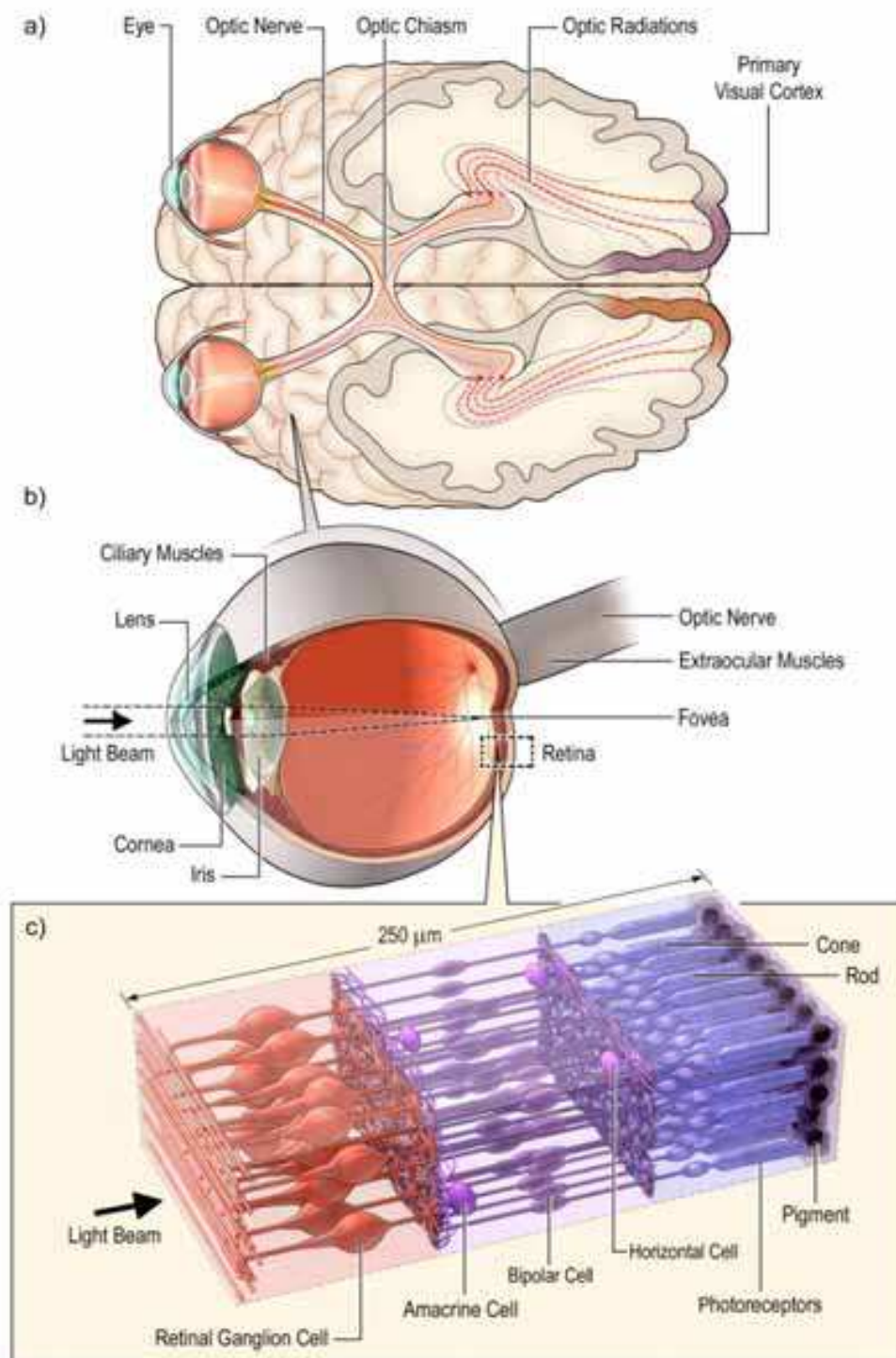
Fig. 20. General view of human brain emphasizing the eyes and primary visual cortex, including: (a) topography of brain; (b) an eye; (c) microscopic view of retina. It should be noted, based on Hubel 1998, that the entire retinal structure (c) is put in the front into the direction of light; so, light needs to go through this structure before it is detected by photoreceptors (retina's "pixels," by analogy to TV camera). It should also be noted that the retina structure is very thin (only 0.25 mm = 250 μm ≅ 10 mils); as in Fig.18(c). This figure is based on analysis in Hubel, 1988

8.2 Cortical neurons

The neural cells have approximately the same structures within retina as well as within cerebral cortex; the most complex of them, however, are *cortical* neurons.

Consider typical *cortical neurons* (Jannson et al., 2009) constituted of the *soma, axons, dendrites,* and *synapses*, in mammals or more generally in vertebrates, as discussed in general neurobiology (Fig. 21).
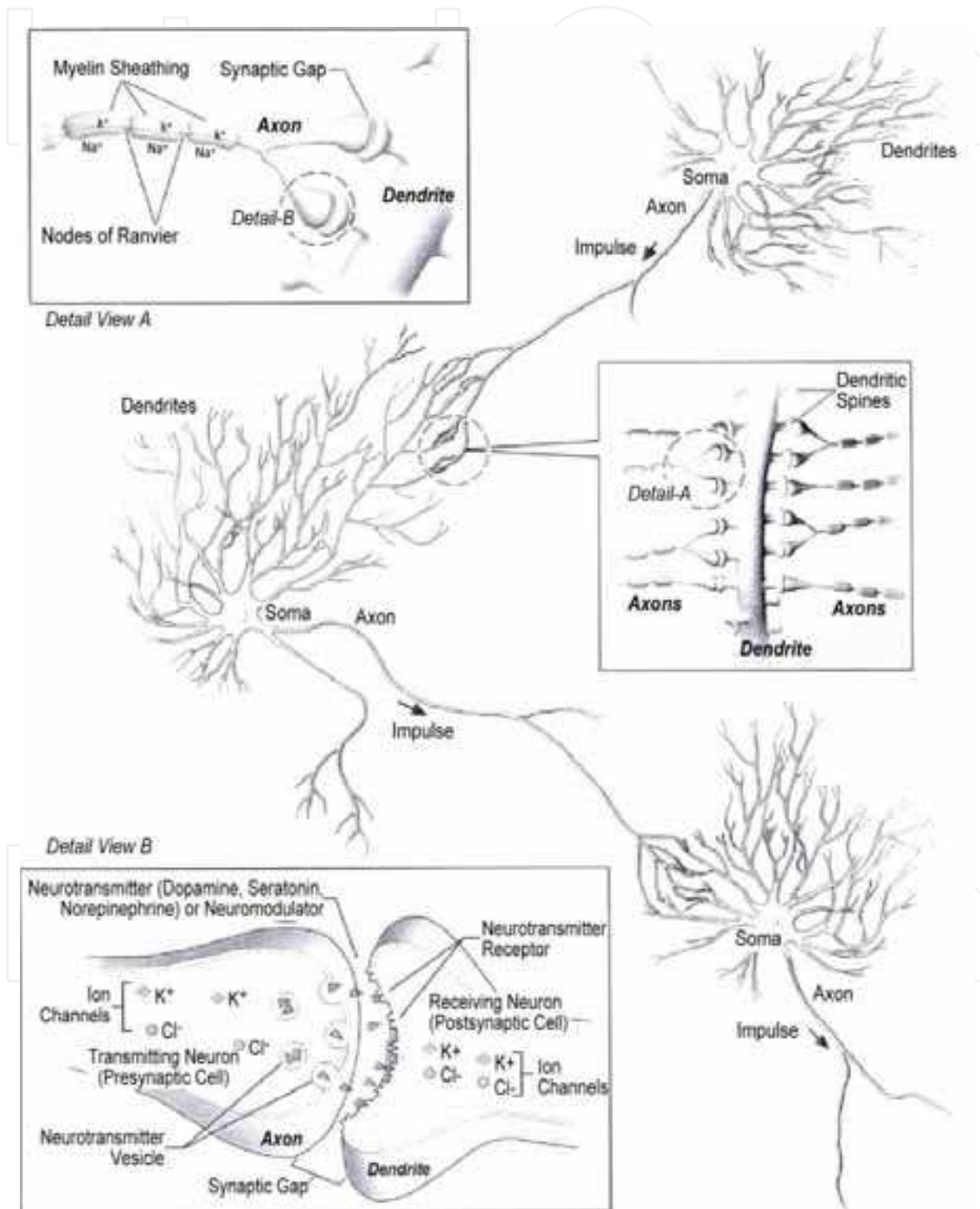

Fig. 21. Schematic of typical cortical neurons, constituted of the soma, axons, dendrites, and synapses, emphasizing the concept of synapse operation, as in Detail View B, from Jannson, et al., 2009

Fig. 21 shows a detailed general schematic of typical cortical neurons emphasizing the concept of operation of the *synapse* and its interconnectivity. More specifically, in Detail View B a synaptic gap between an *axon* and a *dendrite* is shown. We see that in an ion channel, a salt, KCl, is decomposed into positive K+ ions and negative Cl⁻ ions that are transmitted through those channels, which also activate *neurotransmitter vesicles*. These vesicles contain neurotransmitters such as *dopamine* and *serotonin*. Those neurotransmitters allow to preserve propagation of ion current through space (a synaptic gap) into neurotransmitter receptors and then through further ion channels. This ion current (according to Kirchhoff law) flows continuously perhaps as an electron current in a dendrite, which is a kind of wire, rather than a synapse which is an only a gap ("synaptic gap"). Therefore, as we see, typical HE-modeling of synapses analogs differs significantly from that of their natural (biological) equivalents, which are synapses presented as wires rather than gaps (as in Fig. 21), another example of the AA.

According to Fig. 21, the synapses' concept of operation, or CONOPS, is based on slowly varying (hours) **parametric** control of ionic current through a synaptic gap due to *neurotransmitters*, such as *dopamine* or *serotonin*. In other words, the ionic current **mobility** is parametrically controlled due to the presence of neurotransmitters. The physics of ionic current mobility, in general, is well described in Joos, 1986, in the chapter entitled *Electrolytic Conduction*. Assuming equilibrium, or constant-velocity movement, the electrical force: zeE, where z is the ion *valence* (here: z = 1), e is electron charge, and E is electric field intensity in volts cm^{-1}, is equal to *resistance force, f,* proportional to velocity in cm sec^{-1}. This force can be identified with *Stokes' law* (Joos, 1986), as

$$f = 6\pi\eta R_o v \qquad (30)$$

where η is the viscosity coefficient, v is the ion velocity, and R_o is the radius of the *effective ion sphere*. Assuming that, in equilibrium, f = zeE, we obtain the formula for *ion mobility*, in the form (Joos, 1986):

$$u = \frac{v}{E} = \frac{ze}{6\pi\eta R_o} \qquad (31)$$

If we measure these ion mobilities, we obtain, for K+, the mobility value of 67.6·10^{-5} cm sec^{-1}/volt cm^{-1}, which leads to an ionic radius of magnitude 10^{-8} cm = 10^{-4} µm ~1Å, which is the correct order of magnitude. We see, however, that the ionic radii decrease in order: Li-Na-K, rather than increase, according to well-founded results of atomic physics. The reason is that a small ion has a stronger surface force than a large one. This field causes the attachment of molecules of the solvent, thus, reducing mobility, equivalent to increasing effective radius, *R_o*, in Eq. (30).

In summary, the CONOPS of natural (biological) *mammalian synapses* has been discussed, within the visualization of natural *cortical neuron* connectivity, shown in Fig. 21, including ion current mobility as described by Eq. (31). In particular, the term of "synapse" should be considered in terms of synaptic gap (see Fig. 21), rather than as a kind of wire, the latter term being better fitted to dendrites of dendritic neurons, for example. In other words, a synapse, or rather a synaptic gap, is a basic connectivity element between different neurons, which constitute natural (NE) neural networks.

8.3 NE-based contour imaging

The *retinal ganglion* cells are the first cells performing a kind of *image processing*: responding, by firing of short (sub-milisecond) impulses (spikes) with variable frequency: *higher* if response is positive, <u>lower</u> if negative. (This type of cell's response is characteristic for all neural cells in the brain.) There are two types of retinal ganglion cells: *on-center* and *off-center* cells (Hubel, 1988); the first type responding positively to bright spots, while the second type responding positively to dark spots (their numbers are in 50/50 proportion, matching the natural habitat (dark objects are probably just as common as light ones (Hubel, 1988)). In general, no positive response has been observed for uniform diffuse light; only spatial edges with black/white contrast produce positive responses.

The role of neural *synapses* (see Section 8.2) and *neurotransmitters* is such that they are enabling high plasticity of *brain cortex*: synapses can be produced and also killed. Their transmittivity can be regulated by *neurotransmitters* such as *seratonin* (Fig. 21). Also, *inhibitory* synapses are about as plentiful as *excitatory* ones. (The excitatory synapses react positively to increasing some transmitter dose, while the same transmitter can react negatively in inhibitory synapses.) Also, the *amacrine* cells seem to be sensitive to motion (Hubel, 1988).

All the above specializations of ganglion cells lead to a kind of their collective response, emphasizing *contour* (edge/border detection of an object, both static and *on-the-move* (OTM)), including even *edge enhancement*. This tendency continues in the case of *cortical cells*, including a *famous experiment by Hubel and Wiesel in 1958, when, after comprehensive search to register cells' response into the artificial dot, they found, to their surprise, that the neural cells in question produced positive response <u>not</u> to this dot but rather to the sharp but faint shadow cast by the edge of the glass substrate used only for this experiment support.*

Further cell specialization is introduced by the cortical neural cells that respond to "*line*" *stimulus*, reacting positively to line's <u>specific</u> length and orientation. They are not only excitatory and inhibitory but also so-called *complex* and *simple* ones (Hubel, 1988). Their **collective** response can be summarized into positive response into not only specific line's length and orientation but also to its curvature and even its manifold surface topology, related to *catastrophe theory* (Ternovskiy et al., 2002).

The role of the *fovea* is emphasized by the spontaneous *saccadic* eye movement that performs random tiny so-called *microsaccades* that occur several times per second in order to detect any sharp contours (edges) and movements of objects within a given natural scene (Hubel, 1988).

8.4 Relations to HE-based video processing

Given the *NE-based contour imaging* (NECI), as in Section 8.3, we see the basic similarities and differences between the NECI and the HE-based video processing. The similarities are with *Artificial Retina* (Alteheld et al., 2007 & Cheng, 2008) **hard-wired HE-solutions**, simulating ganglion cells and some types of cortical cells, while software-defined pre-ATR HE-solutions (Jannson & Kostrzewski, 2006a) are entirely different, since they do not follow the idea of specialized neural cells. Rather, they are based on *wavelet transform pixel's clusterization* (decimation) (Jannson & Kostrzewski, 2006a), and pixel-by-pixel *Full-Frame-to-Frame Comparison* (FFTFC), as in Jannson, 2001, where also new electronic hardware, based on highly dedicated RISC (*Reduced Instruction Set Computer*) processor is applied.

In the FFTFC case, the *Novelty Filtering* (NF) has been introduced that provides object's *edge-enhancement* in both **temporal** and **spatial** domains. In the temporal domain, applicable to the OTM objects, two sequent video frames are compared by pixels' intensity subtraction, using high intensity *contrast* at object boundary (contour). This is *real-time* (RT) video processing in contrast to the previous ATR (*Automatic Target Recognition*), based on *Fourier transform* (Goodman, 1968), which is not real-time. The NF-operation can also be performed

at **spatial** domain, when frame translation is introduced in electronic domain (Jannson et al., 2007b) as in Fig. 22.

In contrast, in the HE-based hard-wired case, the response specificity is very high. In particular, in Hubel, 1988, Figure in p. 41, the *on-center* ganglion cells' response into small (optimum size) bright spot stimulus is presented, versus dark field (no stimulus). In the latter case (no stimulus) the firing pattern <u>does</u> exist but there is no changes ("no changes" – pattern, or "small changes" will also be in the case of non-optimum size spots (Hubel, 1988)). In the case of stimulus presence, the response is positive (random frequency of pulses <u>increases</u>). It should be emphasized that the positive response is only for the specific stimulus (an object) shape and, only, for small set of specialized ("on-center") ganglion cells. Therefore, indeed, the <u>response specificity is very high</u>. On the other hand, in the case of HE-based software-defined video processing (Fig. 20), the <u>response specificity is low</u>; i.e., the NF-effect is equally effective for widely different object contours, and it can work in both temporal and spatial domains.
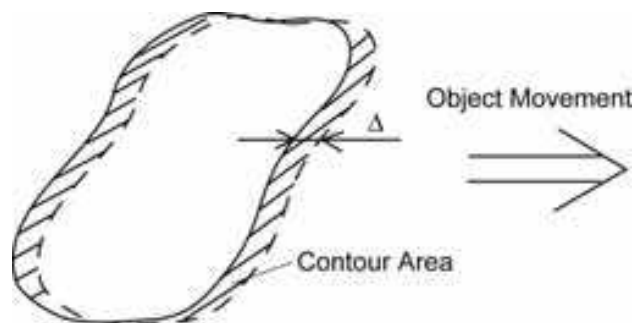

Fig. 22. Pixel-by-pixel subtraction of an object (continuous line), moving from left to right, translated (broken line) by Δ-value during frame-to-frame comparison. Amplified by Novelty Filtering (NF), the object contour area is visualized by the hatched lines

8.5 Holographic associative memory as an example of artificial abstraction

According to Goodman, 1968, the *cross- correlation theorem* has the form:

$$\hat{F}\{\iint U(x',y')V*(x'-x,y'-y)dx'dy'\} = G(f_x,f_y)H*(f_x,f_y) \tag{32}$$

where $\hat{F}\{\iint U(x,y)\} = G(f_x,f_y)$ and $\hat{F}\{V(x,y)\} = H(f_x,f_y)$ are 2D Fourier transforms (see: Eq. (22)). According to Gabor (Jannson et al., 1986), in the case of "noise-like" functions, U and V, that correlate sharply (or, only their fragments correlate sharply), the cross-correlation function takes the form of Dirac-delta function:

$$\iint U(x',y')V*(x'-x,y'-y)dx'dy' = \delta(x,y) \tag{33}$$

Where
$$\delta(x,y) = \begin{cases} \infty, \text{ for } x = 0, y = 0 \\ 0, \text{ for } x \neq 0, y \neq 0 \end{cases} \tag{34}$$

The **cross-correlation** operation (32) takes place in the case of *holographic memory* with object function, U(x,y), stored during holographic <u>recording</u> process while the other object function, V(x,y), is applied during holographic <u>reconstruction</u> process (similar to Vander-Lugt filtering (Goodman 1968)). Therefore, if many $U_i(x,y)$-functions (pages) are stored, where: i = 1, 2, .., M; then, only those pages will be reconstructed which have the same *phrase* (graphical, or textual), as has V(x,y)-function. This is the basis of new highly parallel *query paradigm*, unknown in the

electronic domain, being possible base of future computer search engines with tremendous search capacity. Assume, for example $M = 10^6$, and 10^6-bits per holographic page. Then, if a given graphical/textual phrase is searched in the holographic domain, this phrase can be found, almost instantly (within, say, 10^{-4} sec), amongst: $10^6 \times 10^6 = 10^{12}$ bits; i.e., the *search speed* of this new *computer search engine* will be: 10^{12} bits/10^{-4} sec = 10^{16} bits/sec (!).

Some authors have speculated (Jannson et al., 1986) that this kind of holographic associative memory, un-localized in nature (since the holographic storage is distributed all over the entire hologram volume) can be found in the human brain. However, in the view of <u>hard-wired</u> architecture of visual cortex (see Section 8.4), it would be hard to believe that this is a right guess (rather, such concept is closer to software-defined HE-based architectures; see Fig. 23, for comparison). Therefore, we can identify this AA as an indirect one (see Section 9).

The other AA, directly related to hard-wired NE-based architecture, is presented in Jannson et al., 2009. Based on (voltage) signal propagation in *dendritic neurons*, the proposed *neural lensing* follows, mathematically, Fourier heat conduction analysis, generalized by Lord Kelvin (1850) into cable theory, resulting in *descrete lens focusing principle*. It is too early to predict if it is possible to have this AA-concept to be confirmed by any neurobiological experiments. Nevertheless, this principle can explain such well-known neurobiological phenomenon as the criticality of some neurons in specific human face recognition, without the necessity of differentiating their biologic structure.

9. Conclusions

This paper is a kind of interdisciplinary essay discussing the relationships between animal eyes and relevant *human engineering* (HE), in the context of video surveillance. We purposely use engineering language rather than biologic one in order to make those relationships more familiar to video imagery scientists and engineers, including some necessary simplifications (and repetitions) which would be rather improper if addressed to neurobiological vision auditory. This paper is mostly based on two excellent monographics (Land and Nilsson, 2002, and Hubel 1988), as well as on a number of papers, representing work at Physical Optics Corporation (POC), especially including Jannson et al., 2007.

A number of basic conclusions can be made from this on-animal-eyes essay, namely, relationships between biologic evolution (called here: *Natural Engineering*, or NE), and *Human Engineering* (HE) are quite complex yet they can graphically be presented in the form of two crossing sets, as shown in Fig. 23, where the sets' cross-section is represented by a kind of *technology transfer*, called here *Artificial Abstraction* (AA) (which, obviously, can be only one way; this is why the set framework presented here makes sense). While still using this formal language, we can say that the AAs can be of two kinds: **direct** (with positive connotation) and **indirect** (with negative connotation). The first one is made by conclusion from direct observation of NE-process, with some possible HE-additions that can be made, however, only <u>after</u> direct NE-observation. The second one is made in inverse sequence; i.e., first to make the AA observation and then to find a proper biologic analogy. We hope that during the course of this essay, we have made clear why this indirect AA is usually unsuccessful (see, for example, Section 8.5). Briefly, this is because, while making the indirect AA, we are not able to predict some hidden biologic functions which, nevertheless, are essential for survival of biological organisms, yet they look unimportant for the HE-process.

The best example of this paradox is, perhaps, the role of **pigment** during 500 million years long evolution of animal eyes, from the "first" one (Fig. 1), to the "last" one (Fig. 20). We see that this role is so important (not only for protecting the interior of animal body against deadly UV photons, but also for restoring eye vision after eye's bleaching) that the pigment

entirely occupies one (internal) side of the retina; thus, leaving only the second (external) side available for other vision functions; thus, creating **blocking view** problem, which lingers on through the entire eye evolution.

The other important conclusion is light habitat's or CONOPS' influence on eye evolution, namely, *bifurcation* of *imaging eye* concept into **compound** (*superposition*) one and **elementary** (vertebrates) one, the first one dictated by the requirement of panoramic view (such as in lobster eye; see Section 3), while the second one dictated by the high resolution requirement.

Finally, in the context of moving objects' vision (related to video imagery), we should observe almost complete disparity between NE and HE, namely the NE-based *hard-wired* solution vs. HE-based *software-defined* solution, as discussed in Section 8.4.
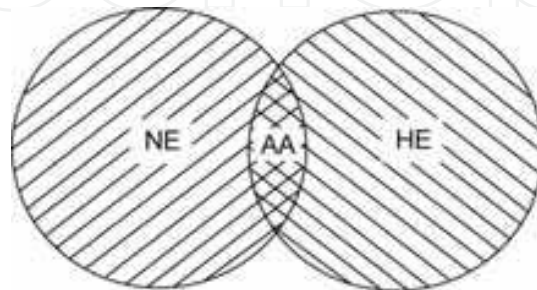

Fig. 23. Illustration of relationship between Natural Engineering (NE), Human Engineering (HE) and Artificial Abstraction (AA), the later one as sets cross-section

We believe this essay has shown the principal role of CONOPS (or, *light habitat*, using biologic language) in the animal eye designs, which, we hope will transfer to more efficient video designs in the future.

10. Acknowledgments

11. References

Alteheld, N.; Roessler, G. & Walter, P. (2007). Towards the bionic eye – the retina implant: surgical, opthalmological, and histopathological perspectives, *Acta Neurochir. Suppl.*, Vol. 97 (Pt. 2), pp. 487-493.

Baker, S. & Nayar, S.K. (1999). A Theory of Single-Viewpoint Catadioptric Image Formation, *Int. J Comp. Vision*, Vol. 35, No. 2, pp. 175-196.

Born, M. & Wolf, E. (1999). *Principles of Optics*, Cambridge University Press, ISBN: 0-5216-4222-1, Cambridge, UK.

Brainard, G.C.; Manifin, J.P.; Greeson, J.B.; Byrue, B.; Glickman, G.; Gerner, E. & Rollay, A.J. (2001). Action Spectrum for Melatonin Regulation in Humans: Evidence for a Novel Circadian Photoreceptor, *J of Neuroscience*, Vol. 21, No. 16, August 2001, pp. 6405-6412.

Bryceson, K.P. & McIntyre, P. (1983). Image Quality and Acceptance Angle in a Reflecting Superposition Eye, *J Comparative Physiology*, Vol. 151, No. 3, pp. 367-380.

Caulfield, J.; Fu, J. & Yoo, S.M. (2004). Artificial Color Image Logic, *Information Science*, Vol. 167, December 2004, pp. 1-7, ISSN: 0020-0255.

Cheng, J. (2008). Retinal Prosthesis: An Innovative Technology for Treating Blindness. *North American J of Medicine and Science*, Vol. 1, No. 1, pp. 20-21.

Denton, E.J. & Nicol, J.A. (1965). Reflection of Light by External Surfaces of the Herring, *J of the Marine Biological Association of the U.K.*, Vol. 45, pp. 711-738.

Dwight, H.B. (1961). *Tables of Integrals and Other Mathematical Data*, The MacMillan Co., Library of Congress Cat. #61-6419, New York.

Fu, J.; Caulfield, J. & Bond, J.J. (2005) Artificial and Biological Color Band Design as Spectral Compression, *Image and Vision Computing*, Vol. 23, No. 8, pp. 761-766, ISSN: 0262-8856.

Fu, J.; Caulfield, J. & Pulusani, S.R. (2004). Artificial Color Vision: a Preliminary Study, *J Electronic-Imaging*, Vol. 3, No. 3, July 2004, pp. 553-558.

Gertsenshteyn, M.; Grubsky, V., Savant, G., & Jannson, T. (2007). Non-Scanning X-Ray Backscattering Inspection System Based on X-Ray Focusing, *Proceedings of SPIE*, ISSN: 0277-786X/09, April 2007, Bellingham, WA.

Gertsenshteyn, M.; Jannson, T., & Savant, G. (2005). Staring/Focusing Lobster-Eye Hard X-Ray Imaging for Non-Astronomical Objects, *Proceedings of SPIE*, ISSN: 0277-786X/05, Bellingham, WA.

Goodman, J.W. (1968). *Introduction to Fourier Optics*, McGraw-Hill, ISBN: 0-0702-3776-X, New York.

Grubsky, V.; Gertsenshteyn, M., & Jannson, T. (2006). Lobster-eye Infrared Focusing Optics, *Proceedings of SPIE*, ISSN: 0277-786X/06, Bellingham, WA.

Hubel, D.H. (1988). *Eye, Brain, and Vision*, Scientific American Library, ISBN 0-7167-6009-6 (pbk), New York.

Hyvarinen, T.S.; Herrala, E. & dall'Ava, A. (1998). Direct Sight Imaging Spectrograph: Unique Add-On Component Brings Spectral Imaging to Industrial Applications, *Proceedings of SPIE*, pp. 165-175, ISSN: 0277-786X, April 1998, Bellingham, WA.

Jagger, W. (1992). The Optics of Spherical Fish-Lens, *Vision Res.*, Vol. 32, No. 7, (July 1992) pp. 1271-1284.

Jannson, T. & Sochacki, J. (1980a). Primary Aberrations of Thin Phase Surface Lenses, *J Opt. Soc. Am.*, Vol. 70, No. 9, pp. 1079-1085, ISSN: 0740-3232.

Jannson, T. (1980b). Shannon Number of an Image and Structural Information Capacity in Volume Holography, *Optica Acta*, Vol. 27, No. 9, pp. 1335-1344, ISSN: 0030-3909/80/2709.

Jannson, T.; Stoll, H.M. & Karaguleff, C. (1986). The Interconnectability of Neuro-Optic Process, *Proceedings of SPIE*, Vol. 698, pp. 157-169, ISSN: 0277-786X.

Jannson, T.; Tengara, I.; Qiao, Y. & Savant, G. (1991). Lippman-Bragg Broadband Holographic Mirrors, *JOSA A*, p. 371, in: "Fundamental Techniques in Holography," H.I. Bjelkhagen and H.J. Caulfield, (Eds.), *SPIE Milestone Series*, SPIE Press, ISBN 0-8194-4334-4, Bellingham, WA.

Jannson, T.P.; Kostrzewski, A.A., & Ternovskiy, I.V. (2001). Super-Fast Supercomputer Class On-Board Processing for Visual Sensor NMD Applications, *Proceedings of SPIE*, pp. 513-518, 2001, ISSN: 0277-786X/01, Bellingham, WA.

Jannson, T. & Kostrzewski, A. (2006a). Real-Time Pre-ATR Video Data Reduction in Wireless Networks, *Proceedings of SPIE*, pp. 6234 OM-1to 6234 OM-9, ISSN: 0277-786X/06, May 2006, Bellingham, WA.

Jannson, T. & Gertsenshteyn, M. (2006b). Hard X-ray Focusing Optics for Concealed Object Detection, *Proceedings of SPIE*, Vol. 6213, pp. 621302-1 to 621302-12, ISSN: 0277-786X/06, April, 2006, Bellingham, WA,

Jannson, T.; Arik, E.; Bennahmias, M.; Nathan, N.; Wang, S.; Lee, K.; Yu, K. & Poliakov, E. (2006c). Performance Metrics for Integrated Lighting Systems, *Proceedings of SPIE*, 6225B-53, pp. 6225E-1 to 6225E-19, April 2006, Bellingham, WA.

Jannson, T.; Kostrzewski, A. & Paki-Amouzou, P. (2007b). ATR for 3D Medical Imaging, *Proceedings of SPIE*, Vol. 6696-13, pp. 669606-1-11, ISSN: 0277-786X/07.

Jannson, T.; Gertsenshteyn, M.; Grubsky, V.; & Amouzou, P. (2007a). Through-the-Wall Sensor System Based on Hard X-Ray Imaging Optics, *Proceedings of SPIE*, Vol. 6538, pp. 65380A-1 to 65380A-9, ISSN: 0277-786X/07, Bellingham, WA.

Jannson, T.; Kostrzewski, A.; Gertsenshteyn, M.; Grubsky, V.; Shnitser, P.; Agurok, I.; Bennahmias, M.; Lee, K. & Savant, G. (2007c). Animal Eyes in Homeland Security Systems, *Proceedings of SPIE*, Vol. 6538-66, pp. 6538 1R-1 to -10, ISSN: 0277-786X/07.

Jannson, T.; Forrester, T., & Degrood, K. (2009). Wireless Synapses in Bio-Inspired Neural Networks, *Proceedings of SPIE*, Vol. 7347, pp. 73470T-1 to 73470T-13, ISSN: 0277-786X/09, Bellingham, WA.

Joos, G. (1986). *Theoretical Physics*, Dover Publications, ISBN: 0-4866-5227-0, Mineola, NY.

Kogelnik, H. (2001). Coupled Wave Theory for Thick Hologram Gratings, *BSTJ*, p. 44, in: *Fundamental Techniques in Holography*, H.J. Bjelkhagen and H.J. Caulfield, (Eds.), *SPIE Milestone Series*, SPIE Press, ISBN 0-8194-4334-4, Bellingham, WA.

Kompaniets, I. (2010). Private Communication, Physical Optics Corporation, Torrance, CA, October 2010.

Kostrzewski, A.A.; Jannson, T.J., & Kupiec, S.A. (2001). Soft Computing and Wireless Communication, (invited paper), *Proceedings of SPIE*, Vol. 4479, pp. 70-74, ISSN: 0277-786X/01, Bellingham, WA.

Kröger, R.H.; Campbell, M.; Fernald, R. & Wagner, H. (1999). Multifocal Lenses Compensate for Diomatic Defocus in Vertebrate Eyes, *J Comparative Physiology A*, Vol. 184, pp. 361-369.

Land, M. F. & Nilsson, D. E.(2002). *Animal Eyes*, Oxford University Press, ISBN: 0-1985-0968-5, New York.

Luneburg, R. (1964). *Mathematical Theory of Optics*, University of California Berkeley Press, Library of Congress Card #64-19010, Berkeley, CA.

Lythgoe, J.N. & Shand, J. (1989). The Structural Basis for Videscent Colour Changes in Dermal and Corneal Iridophores in Fish, *J of Experimental Biology*, Vol. 141, pp. 313-325.

MacKay, D.M., *Phil Mag.*, Vol. 41, p. 289, 1950.

Margenau, M. & Murphy, G.M. (1976). *The Mathematics of Physics and Chemistry*, Robert K. Krieger Publ. Co., ISBN 0-8827-5423-8, Huntington, New York.

Marshall J. & Oberwinkler, J. (1999). The Colorful World of the Mantis Shrimp, Brief Commentary, *Nature*, Vol. 401, p. 873, October 1999, ISSN 0028-0836.

Maxwell, J.C. (1854). *Cambridge and Dublin Math.*, J., Vol. 8, p. 188.

Nicol, J.A. (1989). *The Eyes of Fishes*, Clarendon Press, ISBN: 0-1985-7195-X, Oxford, U.K.

Raymond, L. (1985). Spatial Visual Acuity of the Eagle Aquila Audax: A Behavioral Optical and Anatomical Investigation, *Vision Research*, Vol. 25, No. 10, February 1985, pp. 1477-1491.

Schever, C. & Kolb, G. (1987). Behavioral Experiments on the Visual Stimuli in *Pieris Brassicae L.* (Lepidoptera)," *J Comparative Physiology A*, Vol. 160, No. 5, pp. 645-656.

Schmitz, M. & Blackmann, M. (1998) The Photomechanic Infrared Receptor for the Detection of Forest Fires in the Beetle *Melanophila Acuminata* (Coleoptera: Buprestidue), *Journal Comparative Physiology A*, Vol. 182, pp. 647-657.

Ternovskiy, I.; Jannson, T. & Caulfield, J. (2002). Is Catastrophic Theory Analysis the Basis for Visual Perception? in: *Three-Dimensional Holographic Imaging*, C.J. Kuo and M.H. Tsai, (Eds.), Wiley, ISBN: 0-471-35894-0, New York.

Vogt, K. (1980). The Optical System of the Crayfish Eye, *J Comparative Physiology*, Vol. 135, pp. 1-9.

X-ray Data Booklet, Lawrence Berkeley National Lab., 2001, Berkeley, California, USA.

Video Surveillance

Edited by Prof. Weiyao Lin

ISBN 978-953-307-436-8

Hard cover, 486 pages

Publisher InTech

Published online 03, February, 2011

Published in print edition February, 2011

This book presents the latest achievements and developments in the field of video surveillance. The chapters selected for this book comprise a cross-section of topics that reflect a variety of perspectives and disciplinary backgrounds. Besides the introduction of new achievements in video surveillance, this book also presents some good overviews of the state-of-the-art technologies as well as some interesting advanced topics related to video surveillance. Summing up the wide range of issues presented in the book, it can be addressed to a quite broad audience, including both academic researchers and practitioners in halls of industries interested in scheduling theory and its applications. I believe this book can provide a clear picture of the current research status in the area of video surveillance and can also encourage the development of new achievements in this field.

How to reference

In order to correctly reference this scholarly work, feel free to copy and paste the following:

Tomasz P. Jannson and Ranjit Pradhan (2011). Animal Eyes and Video Surveillance, Video Surveillance, Prof. Weiyao Lin (Ed.), ISBN: 978-953-307-436-8, InTech, Available from: http://www.intechopen.com/books/video-surveillance/animal-eyes-and-video-surveillance

INTECH
open science | open minds